Laboratory analysis of volcanic ash particles using a 2D video disdrometer

Sung-Ho Suh[1], Masayuki Maki[2*], Masato Iguchi[3], Dong-In Lee[1],
Tatsuya Momotani[4], and Akihiko Yamaji[4]

Institutional addresses:

[1]Department of Environmental Atmospheric Sciences, Pukyong National University, Namgu, Busan, Republic of Korea

[2]Research and Education Center for Natural Hazards, Kagoshima University, Korimoto, Kagoshima, Japan

[3]Sakurajima Volcano Research Center, Disaster Prevention Research Institute, Kyoto University, Sakurajima, Kagoshima, Japan

[4]Japan Weather Association, Higashi-Ikebukuro, Toshima-ku, Tokyo, Japan

* Corresponding author: Masayuki Maki (maki@gm.kagoshima-u.ac.jp)

Key Points: Volcanic ash, 2DVD, aerodynamic properties, laboratory experiments

The English in this document has been checked by at least two professional editors, both native speakers of English. For a certificate, please see:

http://www.textcheck.com/certificate/7pU3Ux

Abstract

Radar variables of volcanic ash clouds are dependent on microphysical processes and can be expressed using physical parameters of volcanic ash particles, such as terminal velocity, axis ratio, and canting angle, which are necessary for quantitative ash-fall estimations. In this study, free-fall experiments of volcanic ash were accomplished using a two-dimensional video disdrometer under controlled conditions.

Samples containing a rotating symmetric axis were selected and divided into five types according to shape and orientation, i.e., oblate and prolate spheroids with horizontally and vertically oriented axes and spheres. The horizontally and vertically oriented particles were present in proportions of 75.5% and 21.6%, and oblate and prolate spheroids were in proportions of 76.2% and 23.8%, respectively. The most common shape type was a horizontally oriented oblate spheroid (57.3%).

The terminal velocities were classified according to shape type. The terminal velocities of prolate spheroids (vertically oriented) particles were higher than those of oblate spheroids (horizontally). Terminal velocities were in the range $0.5 <$ volume–equivalent spherical particle diameter (D) < 1 mm for OH because of an increase in axis ratio and a sharp decrease in sample size from $D < 0.7$ mm. The axis ratios fell over a wide range, from 0 to 1.5, at $D < 2$ mm, but converged to 0.94 at $D > 2$ mm.

The histogram of canting angles followed unimodal and bimodal distributions with respect to horizontally and vertically oriented particles, respectively. The mean values were close to 0° and the standard deviation for the entire particle shape types was close to that of raindrops (10°) under calm atmospheric conditions.

1. Introduction

Volcanic eruptions are ~~considered~~ one of the most severe types of natural disasters, and can lead to human casualties and property damage (Wilson et al., 2012; Hillman et al., 2012; Sigurdsson et al., 2015; Wilson et al., 2015). Following an eruption, fine airborne volcanic ash flows for several tens of kilometers, which can cause major problems by increasing aviation traffic (e.g., Bonadonna et al., 2012; Langmann et al., 2012); this was seen after the eruption of Eyjafjallajökull volcano in Iceland during the period April 14– 21, 2010, for example (Bonadonna et al., 2011). From the viewpoint of volcanological hazard reduction, trajectory modeling of volcanic ash clouds is an important research topic. The aim of numerical forecasting modeling is to accurately predict the transport and deposition of ash, which is vitally important for hazard mitigation (Poulidis et al., 2017). Current numerical simulations consider the terminal velocity (V_T) of particles and incorporate wind advection, atmospheric diffusion, and particle aggregation (Folch, 2012; Bonadonna et al., 2015). The V_T of a particle is affected by its shape, density particle volume fraction, and atmospheric properties, such as air pressure (P), temperature (T), and vertical flow (Wilson and Huang, 1979; Haider and Levenspiel, 1989; Ganser, 1993; Bonadonna et al., 1998; Riley, 2003; Dellino, 2005; Coltelli et al., 2008; Alfano et al., 2011; Del Bello et al., 2017). Observational analysis would be helpful for improving the performance of eruption models; however, there is limited information on the microphysical characteristics and inner structures of volcanic ash clouds (Marzano et al., 2006; 2012). Transport and sedimentation of volcanic ash are complex processes, and the residence time and fall velocity of ash is critically dependent on particle size (Bonadonna et al., 1998), where with respect to the latter, smaller particles could be flowing in the atmosphere further from the vent. Ash consists of very fine-grained fragments, volume-equivalent spherical particle diameter (D in mm) is generally smaller than 2 mm, and these are generally dominated by broken glass shards rather than crystal and lithic fragments. Bombs, resulting from larger eruptions, may show vesicularity; they exhibit flexibility similar to plastic when a volcano becomes active and erupts (Sparks et al., 1997; Marzano et al., 2006; 2012). The trajectories of volcanic ash clouds can be detected by meteorological satellites (Stevenson et al., 2015), and the ash amounts can be observed using a ground-based paper cup and an electronic balance (Tajima et al., 2015, Maki et al., 2016). Covering the middle latitudes of the entire globe, geostationary meteorological satellites are able to detect water clouds over the ocean, even when they are far from land; they are also more capable of detecting the upper layers of weather systems, such as convective cells and typhoons, than other weather observational instruments, albeit with relatively low spatial resolution (a few kilometers). When operating in near-polar orbiting mode, these sensors have higher spatial resolution but are limited by their lower temporal resolution, and only pass over a given area twice per day. Weather radar operates for a similar purpose to that of meteorological satellites, and provides information for determining the volume, mass, and echo top height of weather systems. Short-duration eruptions, i.e., less than 1 hour, can be detected at high spatio-temporal resolution, especially in the early period of an eruption. The temporal resolution of weather radar is a few minutes for a single volume scan, and depends on the observation strategy and radar band. The spatial resolution of weather radar is a few hundred meters and is proportional to the radar frequency. A number of ash cloud detections were reported in several observational cases in the US and Japan (Maki and Doviac, 2001; Maki et al., 2012). Marzano et al. (2013) summarized 28 major explosive volcanic eruptions detected by weather radars from 1970 to 2011.

Harris and Rose (1983) attempted to analyze volcanic ash particle size and total mass using a C-band weather radar. Maki and Doviac (2001) found that a weather radar could measure the radar reflectivity factor (z in mm^6 m^{-3}) of volcanic ash columns and Donnadieu et al. (2012) detected volcanic eruptions using an L-band fixed radar. Marzono et al. (2006, 2012) and Maki et al. (2012, 2014) detected and analyzed volcanic eruptions using weather radars, from theoretical (physical) and experimental (engineering) perspectives. These weather radars were developed to detect hydrometeors with a size range from millimeters to centimeters. Coarse particles ($D < 0.53$ mm) can be detected by weather radars. Coarse volcanic ash particles are deposited rapidly following an eruption within a few tens of kilometers from the vent (Bonadonna et al., 1998; Beckett et al., 2015); however, smaller particles, such as fine ash ($D < 64$ μm), are transported over distances of several thousands of kilometers and cannot be detected by operational weather radar, since the minimum detectable reflectivity (MDR) of radar is inversely proportional to the distance between the radar and the target, and where this depends on the wavelength of the transmitted wave (Sauvageot, 1992; Maki et al., 2016).

Weather radars require detailed information on the following basic parameters: particle size distribution (PSD), particle density (ρ_s in g cm^{-3}), dielectric constant ($|K|^2$), V_T (in m s^{-1}), axis ratio (γ), and canting angle (β in °) to estimate ash amount quantitatively, and these can all be observed by a ground-based instrument. The PSD is controlled by the microphysical processes of the volcanic eruption system and plays an important role in its development; it is also essential for accurate evaluation of the backscattering and absorption of particles (Seliga and Bringi, 1976; Marzano et al., 2006; 2012), which affect the radar variables. There are two basic PSD models: i) the gamma size distribution following the gamma function (Γ) and ii) the Weibull size distribution, mainly applied as a log-normal PSD. The former is as a well-known reference in radar meteorology. For precipitation, several raindrop size distribution (DSD) models can be used in a variety of cases (e.g., Ulbrich, 1983; Testud et al., 2001). This implies that a disdrometer is necessary to analyze the observed radar variables and evaluate them in a scattering simulation.

The ashfall rate (R_A) can be also defined in terms of the V_T and is determined by ρ_S, shape, and orientation (Ganser, 1993; Hölzer and Martin Sommerfeld, 2008; Mandø and Rosendahl. 2010; Bagheri and Bonadonna, 2016; Dioguardi et al., 2017). The V_T of particles vary widely due to their irregular shapes and material components (e.g., Wilson, 1972; Harris and Rose, 1983; Bonadonna et al., 2011, Maki et al., 2016)

Volcanic ash particles have a range of shapes, and this presents a major challenge when analyzing their characteristics. To address this, Böhm (1989) analyzed the aerodynamic properties of an irregular hydrometeor and Huang (2010, 2015) applied this concept to snow particles. Recently, the irregularity of volcanic ash particles was analyzed in detail based on the features of various regular particles, such as cubes, cylinders, and disks (Bagheri and Bonadonna, 2016), using a computed tomography (CT) scanner (Dioguardi et al., 2017; Garboczi et al., 2017).

The particle shape observed by radar depends on oscillation or tumbling and can be expressed quantitatively using the β. Research on the β of volcanic ash based on meteorological radar is scarce. Marzano et al. (2012) assumed that the standard deviations of the canting angle (σ_β) were 30° and 10° under unstable conditions (in which the tumbling phenomenon may occur) and stable conditions, respectively. For the case of raindrops, the mean value of the canting angle ($\bar{\beta}$) is close to 0° and σ_β ranged from 4° to 10° (Beard and Jameson, 1983; Hendry et al., 1987; Huang et al., 2008; Ryzhkov et al., 2011). Solid hydrometeors, such as snowflakes and hail, exhibited different features compared to the liquid phase. The σ_β values for graupel, rimed particles, and aggregations were 20°, 16°, and 13°, respectively (Garrett, 2015). Hail that occurs in the context of the tumbling phenomenon is described by $\bar{\beta} = 60(1\text{-}f_w)$, where f_w is the wetting ratio (Synder et al., 2013; Jung et al., 2008). It is assumed that the existence of a liquid phase water covering on the particles reduces the tumbling/oscillations phenomenon.

The $|K|^2$ of the particle depends on the chemical components and phase. Water and ice hydrometeors have quite different values of $|K|^2$, of 0.93 and 0.19, respectively, where the value depends on the radar frequency and T. Volcanic ash has a silicate content proportional to the $|K|^2$, resulting in various values of $|K|^2$, such as 0.34 and 0.39 ± 0.02 (Adam et al., 1996; Marzano et al., 2006; Oguchi et al., 2009).

Aerodynamic properties are important for safe aviation, and for studying the effects of volcanic ash on climate change, since these parameters determine the residence time of ash particles in the atmosphere (e.g., Folch et al., 2009). There are two approaches to studying these aerodynamic properties. The first approach is physical, where a numerical simulation model is used to calculate terminal velocities, drag force, and Reynolds number (Re); examples of this approach can be found in Happel and Brenner (1983). Scattering simulations of particles may be aided by the results of the present study, allowing accurate detection of ash fall by weather radar; this could help verify observed radar variables. In particular, the T-matrix scattering simulation developed by Waterman (1965, 1971) is useful for calculation of the theoretical backscattering power of non-spherical particles. The second approach is related to engineering research, in which the aforementioned relationships are determined experimentally; examples of this approach can be found in Dellino et al. (2005), Bagheri et al. (2013), Bagheri and Bonadonna (2016), and Dioguardi et al. (2018). Particle dispersion depends on atmospheric conditions, such as T and wind, which can affect the retrieval of basic parameters. It is suggested that these parameters be analyzed through free-fall laboratory experiments, to reduce unknown information and obtain reliable results.

The present study focuses on the second approach, and its purpose is to analyze the physical parameters of volcanic ash particles statistically using a ground-based disdrometer, and to develop quantitative ash-fall estimation (QAE) methods for accurate detection of volcanic ash clouds by weather radar. The rest of this paper is organized as follows. Section 2 introduces the free-fall experiment for samples collected with a ground-based disdrometer and the classification method for particle shapes. Section 3 presents the V_T, γ and β results for each type of volcanic ash particle shape. Section 4 summarizes the results.

2. Data and Methods

a. Two dimensional (2D) video disdrometer

The 2D video disdrometer (2DVD) was developed by Joanneum Research (Graz, Austria) to detect single raindrop particles, and the instrument has been modified to cover the errors caused by turbulence effects (Nešpor et al., 2000). The device is able to observe the shape, V_T, and β of a single particle using optical light. The ability to analyze a single particle is a significant advantage compared to other disdrometers, such as the Joss-Waldvogel disdrometer (JWD), the Precipitation Occurrence Sensor System (POSS), and Parsivel (PARticle Size and VELocity). For instance, Parsivel considers a fixed measurement area without any consideration of particle shape (e.g., Tokay et al., 2014), while 2DVD observes particles by passing them through a 100 cm^2 observation area consisting of two light sources and reflecting mirrors and two cameras, one set 6.2 mm above the other, and collects data with a resolution of 630 pixels; this results in a pixel size of 0.2 mm at 55 kHz (Kruger and Krajewski, 2002). Particles passing through the observation area yield shape information according to the radiation intensity of the light sources, which is helpful for calculation of γ and β. The V_T of particles is calculated using the height difference between the two cameras. Based on these advantages, the oscillation and particle shape of raindrops can be analyzed by 2DVD (Thurai and Bringi, 2005; Thurai et al., 2007). Huang et al. (2010, 2015) used 2DVD to analyze the features of irregularly shaped snow. There have been few previous aerodynamic analyses of volcanic ash particles performed using 2DVD, which is able to detect and analyze volcanic ash particles with a range of irregular shapes. Thus, 2DVD offers a unique approach as a new observation strategy.

b. Definition of particle shape type

Volcanic ash particles have various shapes that can be detected by 2DVD (Fig. 1). In the case of raindrops, the DSD is dependent upon the break-up and coalescence processes occurring via up and downdrafts, since the forces of gravity and buoyancy can easily affect raindrop shapes (Rosenfeld and Ulbrich, 2003). Solid particles do not readily change shape when falling without the influence of forces such as collision. It is thus inferred that many particle shapes would be found in the atmosphere, and that it would be possible to define and classify each particle shape type if we were able to accurately detect a single particle. Thus, the range of γ for solid particles would be expected to be wide compared to that of raindrops, and various values of V_T and β would likely be observed. The γ_x of a particle is defined as the ratio of height to width for the observation direction x, and its representative value is calculated using the geometric means of the two γ (γ_1, γ_2) detected by cameras 1 and 2, respectively (Eq. 1):

$$\gamma_{1(2)} = \frac{\mathrm{Height}_{1(2)}}{\mathrm{Width}_{1(2)}}, \qquad \gamma = \sqrt{\gamma_1 \gamma_2}$$

Eq. (1).

The β is defined as the difference in angle between the rotating symmetric axis and vertical axis. The counter-clockwise (clockwise) movement of the rotating symmetric axis has a positive (negative) value and the entire range is 180° (from -90° to 90°) with 0° as the center.

It is necessary to consider the true axis ratio (γ_T) to correctly define the particle shape (Fig. 2). The apparent axis ratio (γ_A) considers the effect of β but the γ_T does not. The 2D coordinates (x, z) of the particle shape with β are defined as follows:

$$x_A = \mathrm{r}\ \cos(\theta + \beta), \qquad z_A = \mathrm{r}\ \sin(\theta + \beta)$$

$$x_T = \mathrm{r}\ \cos\theta, \qquad z_T = \mathrm{r}\ \sin\theta$$

where subscript A is the coordinate of the original data coordinate considering the β and subscript T is the modified data coordinate. The symbol r refers to the length from the data point to the center and the symbol θ represents the degrees of data coordinates from the positive x axis, which range between 0° and 180°. In this paper, γ stands for γ_A for convenience.

An objective criterion for particle shape type was considered since particle shapes can be highly diverse and irregular (e.g., Bagheri and Bonadonna, 2016, Dioguardi et al., 2017; Garboczi et al., 2017, Dioguardi et al., 2018). In the case of irregular particles, the γ can change according to the observation direction; however, any criterion should be able to define the particle shape types strictly and reliably. To solve this problem, particles with a rotating symmetric axis were the main target of the present study. Therefore, we considered oblate spheroid (O), prolate spheroid (P), and sphere (Sp), which all have a rotating symmetric axes. Among these particle types, the major axes of the oblate and prolate spheroids could be horizontally (H) and vertically (V) oriented with respect to the ground, respectively. Thus, the various particle shapes were divided into five types as follows; OH, OV, PH, PV, and Sp.

To define these particle shape types, a strict definition of the γ_T is required, which can be calculated from ~~the~~ β. As with ~~the~~ γ, the two β values are automatically calculated by 2DVD. In the case where the β is assumed as 0°, the rotating symmetric axis for OH and PV can be defined, since it is observed for any observation direction parallel to the ground. However, in the case of OV and PH particles, the rotating symmetric axis cannot be defined when the observation direction is parallel. In the case where the β is not 0°, γ_T for all particle shape types would not change when oscillation occurs in a direction orthogonal to the observation direction, but it is difficult to estimate both γ_T and β when particle oscillation appears in a direction parallel to the observation direction. The ability to restore the γ_T and β relative to this observation direction is limited, which is one of the main disadvantages of the 2D observation strategy.

Based on these facts, a major β was selected based on the following reasoning: i) a β for the observation direction with lower (higher) γ_T for OH (PV) is selected. ii) in the case of OV (PH), for which the rotating symmetric axis was observed for only one observation direction, β was considered where the value of β had a higher (lower) γ_T than that of the other observation direction. Therefore, β with a lower (higher) γ_T in two observation directions for the case of an oblate (prolate) particle was considered as a meaningful value. The Sp could not have their value of β determined theoretically, because there is the possibility of a rotating symmetric axis in any direction.

After removing β, each particle shape was defined using γ_T (Table 1). Note that a 10% bias range was allowed, to take observational error into account. For example, a particle was considered as a sphere when $0.9 < \gamma_T < 1.1$, which is an applied 10% bias range from $\gamma_T = 1$. In addition, the particle types OH and PV (OV and PH) were classified when the value of $|\gamma_1 - \gamma_2|$ was smaller (larger) than $0.1\gamma_T$, to consider particles with only a rotating symmetric axis.

c. Calculate the terminal velocity for the various particle shape types

The V_T of volcanic ash is required to estimate the R_A (kg m^{-2} s^{-1}) on the ground where this depends on atmospheric density (ρ_g in g cm^{-3}), T, Re, drag coefficient (C_D), D, shape, and ρ_s. Kunii and Levenspiel (1969) developed a theoretical V_T equation:

$$V_T = (\frac{4(\rho_s - \rho_g)gD}{3\rho_g C_D})^{0.5} \qquad (10^0 < Re < 10^4)$$

Eq. (2)

Later, Suzuki (1983) developed a theoretical V_T equation for tephra. Bonadonna et al. (2011) then modified the theoretical V_T equation suggested by Kunii and Levenspiel (1969) with observed ash data, which implied that the result of the theoretical V_T equation could be unsuitable for non-spherical particles. Based on these equations, various C_D equations considering non-spherical particles were subsequently developed. Tran-Cong et al. (2004) developed a new equation for C_D using the function of circularity and Hölzer and Somerfeld (2008) introduced a progressed C_D equation considering two types of sphericity: lengthwise ($\Phi_{||}$) and crosswise ($\Phi_{\perp}$). This equation is as follows:

$$C_D = \frac{8}{Re}\frac{1}{\sqrt{\Phi_{||}}} + \frac{16}{Re}\frac{1}{\sqrt{\Phi}} + \frac{3}{\sqrt{Re}}\frac{1}{\Phi^{3/4}} + 0.42 \quad \times 10^{0.41(-\log(\Phi))^{0.2}}\frac{1}{\Phi_{\perp}}$$

Eq. (3)

The Re is defined as:

$$Re = \frac{\rho_g V_T D}{\mu}$$

Eq. (4)

where μ is the dynamic viscosity (kg m^{-1} s^{-1}), which we assumed to be 1.983×10^{-5} based on atmospheric conditions at a T of 25 °C. Three types of sphericity were defined as follows:

$$\Phi = \frac{\pi D^2}{SA}$$

Eq. (5)

where SA is the surface area of the particle (mm^2). The lengthwise sphericity is defined as the ratio between the cross-sectional area of the volume-equivalent sphere and the difference between half the surface area and the mean of the projected vertical cross-sectional area (A_V) of the particle (Eq. 6):

$$\Phi_{||} = \frac{\pi D^2}{4(0.5 \times SA - A_V)}$$

Eq. (6)

The crosswise sphericity is the same as the lengthwise sphericity, except for the denominator, which includes the projected horizontal cross-sectional area of the particle (A_H), defined as follows:

$$\Phi_{\perp} = \frac{\pi D^2}{4A_H}$$

Eq. (7)

It is noteworthy that the V_T is required to calculate the Re and V_T, which refers to the final product. To solve this problem, the theoretical V_T (Eq. 2) was used as the input value of Eq. 4 until Eq. 2 converged.

d. Sakurajima volcano

Japan has around 10% (110) of all of the active volcanos in the world. Sakurajima (1,117m, 31.58° N, 130.65° E, Kyushu, Japan) is an active volcanic island formed around 13,000 years ago, and its tephra is approximately 57–66 % S_iO_2 Peléan-type. The major eruptions periods of Sakurajima were 1471–1476 (Bunmei era), 1779–1782 (An-ei era) and 1914 (Taisho era). The Japan Meteorological Agency (JMA) reported that the eruption frequency of Sakurajima would increase significantly from 2009 (Maki et al., 2014) and the accumulated ash fall exceeded 3.5 kg m^{-2} in Kagoshima city in 2012 (Maki et al., 2016). The Ministry of Land, Infrastructure, Transport, and Tourism (MLITT) installed an operational X-band radar 10.7 km from the vent, as well as 16 automatic volcanic ash weight measurements, to observe volcanic eruptions in 2011 (Fig. 3).

e. Data collection and reanalysis

The data were collected by automatic volcanic ash weight measurements performed on the Sakurajima volcano (Tajima et al., 2015; Maki et al., 2014; 2016). The free-fall experiments were divided into two types; one was performed for each phi scale ($\Phi = -\log_2 D$) from $\Phi = 3$ to -4 ($0.125 < D < 16$ mm), and the other was not considered on a particle size scale. The former data, expressed by A and B (Type 1), were collected at two sites and reanalyzed by size (Fig. 4); the latter data, expressed as C–E (Type 2), were collected at 18 sites (Table 2). Free-fall experiments on collected volcanic ash particles were carried out in the large-scale rainfall simulator of the National Research Institute for Earth Science and Disaster Prevention (NIED) in Tsukuba, Japan. The collected particles were dropped manually ~~by a manager~~ around 17 m from the ground and re-collected by a third-generation 2DVD (Maki et al., 2016). Half a cup of each sample was dropped for 30 s to stimulate dispersion, and the measurement period was 1 min. To avoid wind effects including turbulence, the 2DVD was surrounded by a 27 m^3 windbreaking wall (Fig. 5).

The free-fall experiments were conducted at intervals of 1 min over 6 h 30 min, as shown in Fig. 6. The number of particles detected by 2DVD was less than 10,000 for 1 min, and the particle size range of The former data set (A, B) was proportional to its phi-scale, since small particles may be observed in collisions or break-up from aggregates. Bonadonna et al. (2011) showed that the dominant distribution areas of volcanic ash particles of $\Phi = 1\sim2$, $1\sim3$, and $3\sim9$ corresponded to around 10, 20, and 30 km from the vent of Eyjafjallajökull, Iceland, respectively. Dellino et al. (2012) reported that the dominant volcanic ash particle size is concentered at $\Phi = 0\sim3$ and $1\sim2$ at 3 and 9 km from the vent of the same volcano, respectively. Based on these studies, the results of the present study represent the range between 2 and 20 km from the vent under natural conditions.

Figure 7 shows the distribution of raw data (the number of data: 274,215) for V_T and γ with D. There were various γ values, from 0 to 2, when the volume-equivalent particle $D < 2$ mm, and most of the data were concentrated near 0. The γ values converged around 1 and their distributional range decreased with D. It should be noted that this feature is different from that of raindrops, where smaller raindrops converge around 1 and gradually decrease with D (Thurai and Bringi, 2005). Beard and Chuang (1987) and Andsager et al. (1999) suggested that these raindrop features denote polynomial relationships (Fig. 7a). The median value with a 0.25 mm D interval corresponded well to the center of the data contour. The median line converged around $\gamma = 0.93$ based on the correlation coefficient value (CC). When this was higher than 0.95 for each D interval, the data converged. According to this condition, the range of $2 < D < 5$ mm was satisfied and the mean value was calculated using these data.

The V_T had a wider range when $D < 2$ mm but the median line corresponded well to the center of the data (Fig. 7b). The line representing the largest amount of data is higher than the V_T of raindrops suggested by Atlas et al. (1973), and lower than the volcanic ash discussed by Bonadonna et al. (2011).

To select a reliable range for particle D, a theoretical terminal velocity equation ($V_{T,Ref}$) corresponding to Eqs. 2–7 was used as the reference. The particle density associated with the eruption of Sakurajima volcano is between 2.43 and 2.59 g cm^{-3} (Oguchi et al., 2009), but the actual particles contain air vacuoles (Van Eaton et al., 2012). This means that the bulk density, including vacuoles, is smaller than the particle density. Therefore, the minimum particle density was considered to be 2.43 g cm^{-3}, and this was used as an input parameter. The atmospheric conditions of T and P were considered using ground observation data from automatic weather stations (AWS), supported by the JMA. The falling height of a particle when D = 4 was lower than that under laboratory conditions when it reached 90% of V_T (13.9 m) (17 m); therefore, the available data range is considered to be $D \leq 4$ mm, and this would satisfy a steady-state oscillation. The detailed equations used in the present study are shown in Appendix A.

f. Quality control procedures

The 2DVD was originally developed to detect raindrop hydrometeors. For this reason, additional quality control (QC) checks were deemed necessary to ensure applicability to non-hydrometeors, such as volcanic ash particles. Specifically, we performed the following two QC procedures for accurate analysis of the data:

i) Particle D > 0.25 mm was selected in consideration of the minimum spatial resolution of 2DVD.

ii) If the major axis observed by 2DVD was 10% longer than that of the value calculated directly based on data coordinates, the data were considered erroneous and thus removed. A 10% bias range was considered based on mathematical error, the irregular particle shape, and the limitation of the spatiotemporal resolution of 2DVD.

iii) Based on the definition of β (Fig. 2), the perfect condition with respect to ellipsoids is satisfied when |β| = 0º (90º) for OH and PV (OV and PH); these values are defined as the center values. However, 2DVD calculated that the β for each particle shape type was concentrated around |β| = 0º (90º) with respect to horizontally (vertically) oriented particles, which correspond to OH and PH (OV and PV). Furthermore, analysis of particles with an orthogonal center angle from 0º is difficult, since they have two center angles (±90º). To address observation errors and enhance the convenience of analysis, all center angles were set to $|\beta| = 0^{\circ}$ and modified to give the representative canting angle, β_R, using the following equation:

$$\beta_R = \beta - \beta_0$$

where β_0 is the orienting angle, defined by the central angle of oscillation. In the case of vertically oriented particles (OV and PV), β_0 could be defined as ±90º. The sign of β_0 follows that of β. After selecting the particle shape types and applying these QC procedures, 19.31% of the data (62,953) remained (Table 1).

3. Results

a. Size and shape distribution

The particle size distribution over the entire volcanic ash sample was skewed leftward, and the particle shape distribution differed with particle size (Fig. 8). The particles were predominantly horizontally oriented (75.51%) or vertically oriented (21.60%). Oblate and prolate spheroids made up 76.26% and 23.85% of the particles, respectively. Hence, the particles were mainly OH (57.38%) or PH (15.88%) (Table 2). The particles were predominantly $0.25 < D < 0.5$ mm (63.00%) or $0.5 < D < 1$ mm (32.80%). Relatively few particles had $D > 1$ mm (4.20%).

There was large variation in shape among particles $0.25 < D < 0.5$ mm, but the variation decreased with increasing D. All of the particle shape types had the largest number of particle at $D > 1.0$ mm and the next were shown at $0.5 < D < 1.0$ mm, except for OH. In total, 95.80% of OH particles had $D < 1$ mm; at $D < 0.5$ mm, the value was 75.68%, and at D = 0.5–1 mm, it was 22.36%. In the cases of PH and OV, 93.63% and 93.87% of these particles, respectively, had $D < 1$ mm. Beyond $D > 1$ mm, the differences in the number of particles for each particle shape type were considerably decreased. The PSD of volcanic ash particles depended on the distance from the vent (Beckett et al., 2015; Stevenson et al., 2015). Based on the results, this particle size and shape distribution would represent the area located over 2–20 km from the vent.

b. Terminal velocity

It is difficult to apply qualitative analysis approaches to V_T since it depends on the scale, magnitude, and duration of an eruption. Furthermore, it is impossible to develop a model of V_T without knowledge of the aerodynamic properties of the volcanic ash particles, since V_T is a function of the density, shapes, and oscillations of particles. In this study, we analyzed the basic features of volcanic ash particles in a laboratory experiment to obtain reliable results.

The observed values of V_T were well classified by particle shape and were generally higher than those of raindrops, as previously suggested by Atlas et al. (1973) (Fig. 9). The values were estimated using a multiple regression analysis, with V_T defined for each particle type, and with additional QC measures applied. If we consider a single V_T QC measure for the entire particle types, a number of available data might be removed, since V_T critically depends on particle shape. Therefore, we applied a ±60% V_T QC threshold (Jaffrain et al., 2011).

The highest values of V_T were recorded in the order of prolate, sphere, and oblate. Vertically oriented particles had higher V_T values than horizontal ones. For raindrops with a single particle shape type, V_T changes with atmospheric conditions, especially vertical air motion (Kim and Lee, 2016). However, the V_T values for volcanic ash particles change independent of external conditions, since they have various particle shapes. The V_T for every particle type was considered to be in a power-law form, except for OH. OH particles followed the regression line relatively closely, and showed the highest CC and root mean square error (RMSE) values, of 0.94 and 0.46 m s^{-1}, respectively. Horizontally orientated particles had relatively higher correlations (OH: 0.94, PH: 0.87) compared to those with a vertical orientation (OV: 0.75, PV: 0.71). All of these data are summarized in Table 3.

To verify the reliability of the particle data obtained by 2DVD, which was originally developed to detect liquid raindrops, particle density, C_D, and Re, as well as theoretical V_T values according to these parameters, were analyzed. To calculate the parameters of interest, including the surface area and cross-sectional area of irregular particles, we applied the irregular particle volume estimation equations of Huang et al. (2010).

c. Aerodynamic properties

Particle densities were estimated using the $V_{T,Ref}$, converged to 2.37 g cm^{-3} when $D < 1.5$ mm (Fig. 10a). This value corresponds well to that of the minimum particle density (2.44 g cm^{-3}) reported by Oguchi et al. (2009). The slight difference is likely due to observation errors and the presence of vesicles (e.g., Seligman et al., 2016). The median value of particle density is changed to $0.5 < D < 1.5$ mm, and this range corresponds to that of V_T. Horizontally oriented particles (OH and PH) have relatively smaller particle density and vertically oriented particles (OV and PV) have higher density (Fig. 10b); spheres have particle densities that accord best with D. The median particle density values for all particle shapes converged when $D < 2$ mm, and the converged particle density values ranged from 2.35 to 2.50 g cm^{-3}.

The Re and C_D for the all particle shapes ranged from 10 to 4,000 and 0.6 to 20, respectively (Fig. 11a). Higher values of C_D were observed when $Re < 70$; above this threshold, C_D dramatically decreased. These results were derived according to the number of OH particles, which mainly had $D < 0.5$ mm, and had higher C_D and lower Re. Particle shape was divided into two types: OH and others (Fig. 11b). OH particles had higher C_D compared to the other particle shapes, which in turn showed few differences among themselves. The OH particles experience strong drag forces under the same flow conditions, leading to lower V_T. The differences between OH and other particles diminished with $Re < 1,000$. The other particle shapes had relatively higher C_D in the range $10 < Re < 3,000$. Rong et al. (2015) analyzed the relationship between Re and C_D for oblate and prolate particles, and showed that OH particles had higher C_D compared to the reference line (Clift and Gauven, 1971) in the range $0 < Re < 400$. Each relationship is summarized in Fig. 11.

d. Axis ratio

The γ of a particle affects the backscattering power of electromagnetic waves, and it is necessary to calculate the horizontal reflectivity (Z in dBZ), differential reflectivity (Z_{DR} in dB), and specific differential polarization phase shift (K_{DP} in ° km^{-1}). Note that previous studies have analyzed the γ distribution for raindrops and snow, including hail; however few studies have been reported on volcanic ash.

Smaller raindrop particles exhibit higher values of σ. However, most of the particles are concentrated around $\gamma = 1$ when D is close to 0 mm, and the γ for raindrops was shown to be inversely proportional to D (e.g., Pruppacher and Beard, 1970; Beard and Chuang, 1987; Goddard et al. 1994b; Andsager et al. 1999; Thurai and Bringi, 2005). Snowflakes showed linear relationships of γ and D that were different from those of raindrops. Brandes et al. (2007) suggested that an equation for γ where (D) = 0.01714D + 0.8467. Hail had a similar γ to snowflakes, of 0.77 (Matson and Huggins, 1980) versus $0.75 < \gamma < 0.79$ (Jewell and Brimelow, 2009), respectively.

Figure 12 shows the quartiles and median values of γ for the entire particle shapes, and for each individual particle shape type. The γ had a higher standard deviation (σ_γ) of > 0.25 when D < 0.75 mm, which decreased and converged to $\sigma_\gamma = 0.15$ when D > 1 mm (Fig. 12a). The γ in the lower σ_γ range converged to $\gamma = 0.94$ and could be expressed as follows:

$$\gamma(D) = 0.94 - 0.25\exp(-1.90\ D) \qquad \text{Eq. (8)}$$

The particles are more easily classified by shape than by V_T (Fig. 12b). Every particle shape type was independent of D, except for OH. The relationships of the particle shape types are expressed as follows (Eqs. 9–12):

$$\gamma(\mathrm{D})_{OH} = 0.37\tanh(1.84\mathrm{D} - 1.88) + 0.38$$

Eq. (9)

$$\gamma_{OV} = 1.15$$

Eq. (10)

$$\gamma_{PH} = 0.88$$

Eq. (11)

$$\gamma_{PV} = 1.24$$

Eq. (12)

The parameter $\gamma(\mathrm{D})_{\mathrm{OH}}$ was calculated using the hyperbolic tangent (tanh) for the following reasons: i) its range of values was wider than those of other particle types; ii) the data distribution changed continuously with D; and iii) it was present in a higher proportion (30.44%) compared to the other parameters. We found that variations in γ decreased with D and the proportion of Sp shapes increased when $D > 2$ mm. The particle types OV and PH showed a wide distribution over $1 < \gamma < 1.5$ and $0.4 < \gamma < 1.0$, respectively, when $D < 2$ mm, but the variability in median values was relatively low. The relationships of γ for each particle shape type could be expressed by constant values at $\gamma = 0.75$ (OH), 0.88 (PH), 1.15 (OV), and 1.24 (PV), respectively, and these differences are around $\gamma = 0.12$. Maki et al. (2014) analyzed dual-pol radar variables and found that Z_{DR} increased with time; the dominant values at 10 and 18 min after the eruption were close to 1 and 2 dB, respectively. With respect to hydrometeors, the dominant γ of volcanic ash can be inferred from the relationship between γ and Z_{DR}, as suggested by Herzegh and Jameson (1992). The values correspond to the γ of volcanic ash when the median γ of rain and ice is 0.85 and 0.73, respectively; this assumption is based on the $|K|^2$ for volcanic ash being between that of ice and liquid water. These representative values correspond to D of 1 and 0.15 mm, respectively, based on Eq. 9. It is implied that the amount of particles was largest when D < 1 mm (95.8%) and the γ corresponded well to the observed Z_{DR}.

e. Canting angle

Statistical analysis of β is required to understand the aerodynamic properties of volcanic ash particles, and the input parameters of T-matrix scattering simulations, to verify the observed radar variables. A histogram was used to analyze the distribution and dominant characteristics of β_R. The interval of the histogram was set to 4°.

More than 95% of β values for each particle shape type were concentrated in the range $|\beta_R| \leq 30^o$, with 0^o as the center (Fig. 13). The particles were symmetrically distributed around 0^o and more than 50% were concentrated in the range $|\beta_R| < 4^o$. The horizontally oriented β distribution was relatively narrow ($|\beta_R| < 20^o$) and exhibited a unimodal distribution. It is noteworthy that 90% of OH particles were concentrated in the range $|\beta_R| < 4^o$. The vertically oriented β distribution was relatively broader ($|\beta_R| < 30^o$) and followed a bimodal distribution. PV exhibited a bimodal form, but this was not symmetrical about 0^o. For spheres, the β distribution was narrower, similar to horizontally oriented particles, and its had a bimodal distribution, similar to vertically oriented particles, indicating that the independent features of both orientations were combined.

The values of $|\overline{\beta_R}|$ and $|\sigma_\beta|$ for OH and PV (OV, PH) were 0^o and 3.5^o (0.4^o, 13.1^o), and 1.3^o and 12.7^o (0.2^o, 10.9^o), respectively. OV (OH) had the highest (lowest) value of $|\sigma_\beta|$. Thus, $|\overline{\beta_R}|$ and $|\sigma_\beta|$ for the all volcanic ash particles were quite similar (0.3^o and 10.1^o, respectively) to those of raindrops and the value of $|\sigma_\beta|$ for Sp (11.5°) was higher than that of the entire data set (10.1°).

In the case OH, the $|\sigma_\beta|$ value was about half that for raindrops while the values for OV, PH, and PV particles were all similar to that of raindrops. This validates the assumption of Marzano et al. (2012)

under stable conditions ($|\sigma_\beta| = 10°$). Therefore, we assumed that the tumbling phenomenon ($|\sigma_\beta| > 30°$) of the particles under calm atmospheric conditions was likely to be minor.

To analyze the correlation between particle D and β, quartiles for each particle D interval were calculated (Fig. 14). The particles were concentrated at $|\beta_R| < 30°$ regardless of D, and median values were stable when D < 1 mm for the entire particle shape types; however, fluctuation increased with D (Fig. 14a). The $|\sigma_\beta|$ values gradually increased from 10° to 13° when 0.3 < D < 1.3 mm and variability was greatest around the center (13°). This increase in $|\sigma_\beta|$ would not be expected in the case of a relatively small number of particles (Fig. 8a), since their standard deviation is largely maintained at about 13° regardless of dataset size.

Variability in the median values for individual particles was more apparent. The values converged around 0° but fluctuation increased with greater D from the zero line. The median $|\beta_R|$ values exceeded 3°, 5°, 10°, and 15° when D > 1 mm, 1 < D < 2 mm, 2 < D < 3 mm, and D > 3 mm, respectively (Fig. 14b).

e. Verification

To verify the basic parameters of volcanic ash estimated in the present study, the $V_{T,\,Ref}$ (Eq. 2) was compared to the observed values (V_T) obtained in the free-fall experiments (Fig. 15). The particle density (Fig. 10) and γ (Fig. 12) estimated in the present study were applied to the C_D (Eq. 3) and the sphericity (Eqs. 5–7) relationships; these parameters were used as input values for $V_{T,\,Ref}$. The atmospheric conditions were the same as in Fig. 5.

There was wide range of V_T over 0.25 < D < 1.2 mm for the entire particle shape types, and V_T decreased when D > 1.2 mm. The V_T in the present study corresponds to that obtained by Miwa et al (2015), who analyzed Parsivel data using the same laboratory experiments (Fig. 5); correspondence was also good with other previous results (Beckett et al., 2015). A polynomial regression analysis was used to explore the nonlinear relationship between V_T and D (Table 3). The inflection point of V_T at 0.7 < D < 1.3 mm results from an increase in the number of OH when D < 1 mm (Fig. 8).

The $V_{T,Ref}$ was lower (higher) than the observed value when D < 1.2 mm (D > 2.4 mm). One of the reasons why a difference between the theoretical and observed values appeared when D > 2.4 mm was that the upper limit of D when 90% of the terminal velocity was reached was set at 4 mm for a height of 17 m (Fig. A1). This is nonetheless meaningful because the values of $V_{T, Ref}$ calculated based on the basic parameters in this study were within ±5% of the observed value.

4. Summary and Conclusions

To inform the development of QAE methods, basic parameters (V_T, γ and β) of volcanic ash particles were analyzed using 2DVD. Data were collected according to 18 automatic volcanic ash weight measurements performed on Sakurajima volcano, Japan (31.58º N, 130.65º E). To identify the aerodynamic properties of the volcanic ash particles in the samples, a free-fall experiment using 2DVD was conducted with the large-scale rainfall simulator of the NIED, and 274,215 raw data points were obtained.

Radar variables are highly dependent on the $|K|^2$, size, and shape of particles. Particle types with rotating symmetric axes were selected, because volcanic ash particles have a wide variety of irregular shapes. Their orientation was also considered, and horizontally (OH) and vertically (OV) oriented oblate spheroids were therefore studied, as well as horizontally (PH) and vertically (PV) oriented prolate spheroids, and spheres (Sp).

The particle shape types were defined according to their γ_T, with a 10% bias range; the β among two values was selected to be representative when the value of γ_T was smaller (larger) than that of the other observation direction in the case of the oblate (prolate) particle.

The dominant particle shape comprised horizontally and vertical oriented particles, present in proportions of 75.51% and 21.60%, respectively. Regarding particle shape, oblate (prolate) spheroids comprised 76.26% (23.85%) of all particles in the samples. The most common particle shape type was OH, accounting for 59% of all particles when $D < 1$ mm, and 69% when $D < 0.5$ mm. Overall, 95.80%, 93.87%, and 93.63% of the OH, OV, and PH particles had $D < 1$ mm, respectively.

The V_T of the particles were in the order of prolate, sphere, and oblate, and vertical oriented particles had higher V_T than horizontal orientated particles. These results are consistent with the $V_{T, Ref}$, which suggests that 2DVD is a reliable for observing volcanic ash particles and the tumbling phenomenon under stable weather conditions. A noticeable increase in V_T for OH in the range $0.5 < D$

< 1 mm occurred through an increase in γ and a decrease in the number of OH when D ~0.7 mm; this was not observed for other particle types.

The estimated ρ_s converged to 2.37g cm^{-3} when D > 1.5 mm, and the median value changed over the range 0.5 < D < 1.5 mm. This is consistent with the particle density value for the Sakurajima volcano reported by Oguchi et al. (2009). The distributions of C_D and Re were divided into two particle type categories, OH and other, and C_D increased dramatically when Re < 70. These results were derived from the particle concentration of OH, which was highest when D < 0.5 mm; at this threshold, C_D was higher and Re was lower. The range of V_T over 0.7 < D < 1.3 mm was informed by both γ and particle density.

The σ_γ decreased when D > 0.75 mm, to 0.15, and converged to $\gamma = 0.94$. This is in contrast to the results obtained for raindrops, but is highly consistent with results for actual eruptions. Most measured values of Z_{DR} for Sakurajima volcanic ash clouds on August 18, 2013 were in the range 1–2 dB, corresponding to a horizontally oriented oblate spheroid.

The $|\sigma_\beta|$ of OV particles with $|\beta_0| = 90^\circ$ was largest (13.1°) among all particle types. OH particles had the lowest $|\sigma_\beta|$ at 3.5°, and this value was also smaller than that of raindrops (7°–10°). Based on the $|\sigma_\beta|$ results, the tumbling phenomenon would not be dominant under calm atmospheric conditions. The quartiles were stable when D < 1 mm for the entire particle shape types, but increased with D. The value of σ_β was higher when D < 1.3 mm and started to converge around 13°due to a decrease in the number of OH particles.

The estimated γ and ρ_s were applied to the $V_{T,Ref}$ for validation. The observed V_T was within ±5% of the theoretical value when $D \leq 4$ mm, implying that the estimates of the basic parameters were reasonable for the particle range considered.

These results could inform the development of new approaches for detecting non-hydrometeors using weather radar, thus facilitating observations of ash clouds and preventing the damage to human life and property caused by large amounts of ash fall. In future work, we will analyze the eruption of Sakurajima volcano that occurred on August 18, 2013 with a dual-pol radar and 2DVD, using basic parameters of volcanic ash particles obtained from laboratory experiments. Differences in characteristics between the experimental, and actual basic parameters, and PSD, will be investigated.

Acknowledgments

This work was supported by a Grant-in Aid for JSPS KAKENHI (grant number JP16H03145) and partially supported by a DPRI collaborative research grant (Kyoto Univ. 25G-11). The authors acknowledge the provision of ashfall data and funding for this work from Kyoto and Kagoshima Universities. The 2DVD data were provided by MEXT, Japan. We also thank the NIED for use of their large-rainfall simulator.

Appendix A

The theoretical fall velocity and falling distance with time are calculated as follows;

$$F = ma = F_g - F_D$$

Eq. (A1)

$$F_g = mg$$

Eq. (A2)

$$F_D = \frac{1}{2}\rho_g V^2 C_D A$$

Eq. (A3)

where F_g is universal gravitation, F_D is drag force, m is mass, and a is the free-fall acceleration. In Eq. A2, g is the acceleration due to gravity, considered to be 9.81 m s^{-2}, and V and C_D in Eq. A3 correspond to the values in Eq. 2–7. The symbols μ and ρ_g are the dynamic viscosity and density of the atmosphere and were assumed as 1.837×10^{-5} kg m^{-1} s^{-1} and 1.194×10^{-5} g cm^{-3}, respectively. The results were based on conditions at an atmospheric T as 25 °C.

To ensure accuracy, we considered the surface roughness effect of a volcanic ash particle (1.07^{-1}) on the fall velocity, as suggested by Bagheri and Bonadonna (2016), and the results for D = 4 mm are shown in Fig. A1.

References

Adams, R. J., Perger, W. F., Rose, W. I., and Kostinski, A.: Measurements of the complex dielectric constant of volcanic ash from 4 to 19 GHz, Journal of Geophysical Research: Solid Earth, 101, 8175-8185, 1996.

Alfano, F., Bonadonna, C., Delmelle, P., and Costantini, L.: Insights on tephra settling velocity from morphological observations, Journal of Volcanology and Geothermal Research, 208, 86-98, 2011.

Andsager, K., Beard, K. V., and Laird, N. F.: Laboratory measurements of axis ratios for large raindrops, Journal of the Atmospheric Sciences, 56, 2673-2683, 1999.

Atlas, D., Srivastava, R., and Sekhon, R. S.: Doppler radar characteristics of precipitation at vertical incidence, Reviews of Geophysics, 11, 1-35, 1973.

Böhm, H. P.: A general equation for the terminal fall speed of solid hydrometeors, Journal of the Atmospheric Sciences, 46, 2419-2427, 1989.

Bagheri, G. and Bonadonna, C.: On the drag of freely falling non-spherical particles, Powder Technology, 301, 526-544, 2016.

Bagheri, G., Bonadonna, C., Manzella, I., Pontelandolfo, P., and Haas, P.: Dedicated vertical wind tunnel for the study of sedimentation of non-spherical particles, Review of Scientific Instruments, 84, 054501, 2013.

Beard, K. V. and Chuang, C.: A new model for the equilibrium shape of raindrops, Journal of the Atmospheric sciences, 44, 1509-1524, 1987.

Beckett, F., Witham, C., Hort, M., Stevenson, J., Bonadonna, C., and Millington, S.: Sensitivity of dispersion model forecasts of volcanic ash clouds to the physical characteristics of the particles, Journal of Geophysical Research: Atmospheres, 120, 2015.

Bonadonna, C., Cioni, R., Pistolesi, M., Elissondo, M., and Baumann, V.: Sedimentation of long-lasting wind-affected volcanic plumes: the example of the 2011 rhyolitic Cordón Caulle eruption, Chile, Bulletin of Volcanology, 77, 13, 2015.

Bonadonna, C., Ernst, G., and Sparks, R.: Thickness variations and volume estimates of tephra fall deposits: the importance of particle Reynolds number, Journal of Volcanology and Geothermal Research, 81, 173-187, 1998.

Bonadonna, C., Folch, A., Loughlin, S., and Puempel, H.: Future developments in modelling and monitoring of volcanic ash clouds: outcomes from the first IAVCEI-WMO workshop on Ash Dispersal Forecast and Civil Aviation, Bulletin of volcanology, 74, 1-10, 2012.

Bonadonna, C., Genco, R., Gouhier, M., Pistolesi, M., Cioni, R., Alfano, F., Hoskuldsson, A., and Ripepe, M.: Tephra sedimentation during the 2010 Eyjafjallajökull eruption (Iceland) from deposit, radar, and satellite observations, Journal of Geophysical Research: Solid Earth (1978–2012), 116, 2011.

Brandes, E. A., Ikeda, K., Zhang, G., Schönhuber, M., and Rasmussen, R. M.: A statistical and physical description of hydrometeor distributions in Colorado snowstorms using a video disdrometer, Journal of applied meteorology and climatology, 46, 634-650, 2007.

Clift, R. and Gauvin, W.: Motion of particles in turbulent gas streams, British Chemical Engineering, 16, 229-&, 1971.

Coltelli, M., Miraglia, L., and Scollo, S.: Characterization of shape and terminal velocity of tephra particles erupted during the 2002 eruption of Etna volcano, Italy, Bulletin of volcanology, 70, 1103-1112, 2008.

Del Bello, E., Taddeucci, J., Vitturi, M. d. M., Scarlato, P., Andronico, D., Scollo, S., Kueppers, U., and Ricci, T.: Effect of particle volume fraction on the settling velocity of volcanic ash particles: insights from joint experimental and numerical simulations, Scientific reports, 7, 39620, 2017.

Dellino, P., Gudmundsson, M., Larsen, G., Mele, D., Stevenson, J., Thordarson, T., and Zimanowski, B.: Ash from the Eyjafjallajökull eruption (Iceland): Fragmentation processes and aerodynamic behavior, Journal of Geophysical Research: Solid Earth, 117, 2012.

Dellino, P., Mele, D., Bonasia, R., Braia, G., La Volpe, L., and Sulpizio, R.: The analysis of the influence of pumice shape on its terminal velocity, Geophysical Research Letters, 32, 2005.

Dioguardi, F., Mele, D., and Dellino, P.: A New One-Equation Model of Fluid Drag for Irregularly Shaped Particles Valid Over a Wide Range of Reynolds Number, Journal of Geophysical Research: Solid Earth, 123, 144-156, 2018.

Dioguardi, F., Mele, D., Dellino, P., and Dürig, T.: The terminal velocity of volcanic particles with shape obtained from 3D X-ray microtomography, Journal of Volcanology and Geothermal Research, 329, 41-53, 2017.

Donnadieu, F.: Volcanological applications of Doppler radars: A review and examples from a transportable pulse radar in L-band, INTECH Open Access Publisher, 2012.

Folch, A.: A review of tephra transport and dispersal models: evolution, current status, and future perspectives, Journal of Volcanology and Geothermal Research, 235, 96-115, 2012.

Folch, A., Costa, A., and Macedonio, G.: FALL3D: A computational model for transport and deposition of volcanic ash, Computers & Geosciences, 35, 1334-1342, 2009.

Ganser, G. H.: A rational approach to drag prediction of spherical and nonspherical particles, Powder Technology, 77, 143-152, 1993.

Garboczi, E. and Bullard, J.: 3D analytical mathematical models of random star-shape particles via a combination of X-ray computed microtomography and spherical harmonic analysis, Advanced Powder Technology, 28, 325-339, 2017.

Garrett, T. J., Yuter, S. E., Fallgatter, C., Shkurko, K., Rhodes, S. R., and Endries, J. L.: Orientations and aspect ratios of falling snow, Geophysical Research Letters, 42, 4617-4622, 2015.

Goddard, C. and Wierzbicka, A.: Semantic and lexical universals: Theory and empirical findings, John Benjamins Publishing, 1994.

Hölzer, A. and Sommerfeld, M.: New simple correlation formula for the drag coefficient of non-spherical particles, Powder Technology, 184, 361-365, 2008.

Haider, A. and Levenspiel, O.: Drag coefficient and terminal velocity of spherical and nonspherical particles, Powder technology, 58, 63-70, 1989.

Happel, J. and Brenner, H.: Low Reynolds number hydrodynamics: with special applications to particulate media, Springer Science & Business Media, 2012.

Harris, D. M. and Rose, W. I.: Estimating particle sizes, concentrations, and total mass of ash in volcanic clouds using weather radar, Journal of Geophysical Research: Oceans (1978–2012), 88, 10969-10983, 1983.

Hendry, A., Antar, Y., and McCormick, G.: On the relationship between the degree of preferred orientation in precipitation and dual-polarization radar echo characteristics, Radio science, 22, 37-50, 1987.

Herzegh, P. H. and Jameson, A. R.: Observing precipitation through dual-polarization radar measurements, Bulletin of the American Meteorological Society, 73, 1365-1376, 1992.

Hillman, S. E., Horwell, C. J., Densmore, A. L., Damby, D. E., Fubini, B., Ishimine, Y., and Tomatis, M.: Sakurajima volcano: a physico-chemical study of the health consequences of long-term exposure to volcanic ash, Bulletin of volcanology, 74, 913-930, 2012.

Huang, G.-J., Bringi, V., Cifelli, R., Hudak, D., and Petersen, W.: A methodology to derive radar reflectivity-liquid equivalent snow rate relations using C-band radar and a 2D video disdrometer, Journal of Atmospheric and Oceanic Technology, 27, 637-651, 2010.

Huang, G.-J., Bringi, V., Moisseev, D., Petersen, W. A., Bliven, L., and Hudak, D.: Use of 2D-video disdrometer to derive mean density–size and Z e–SR relations: Four snow cases from the light precipitation validation experiment, Atmospheric Research, 153, 34-48, 2015.

Huang, G.-J., Bringi, V., and Thurai, M.: Orientation angle distributions of drops after an 80-m fall using a 2D video disdrometer, Journal of Atmospheric and Oceanic Technology, 25, 1717-1723, 2008.

Jaffrain, J., Studzinski, A., and Berne, A.: A network of disdrometers to quantify the small-scale variability of the raindrop size distribution, Water Resources Research, 47, 2011.

Jewell, R. and Brimelow, J.: Evaluation of Alberta hail growth model using severe hail proximity soundings from the United States, Weather and Forecasting, 24, 1592-1609, 2009.

Jung, Y., Zhang, G., and Xue, M.: Assimilation of simulated polarimetric radar data for a convective storm using the ensemble Kalman filter. Part I: Observation operators for reflectivity and polarimetric variables, Monthly Weather Review, 136, 2228-2245, 2008.

Kanofsky, L. M.: A comparative study of drop size distribution retrieval using two video disdrometers and a UHF wind profiling radar, 2005.

Kim, D. K. and Lee, D. I.: Raindrop size distribution properties associated with vertical air motion in the stratiform region of a springtime rain event from 1290 MHz wind profiler, micro rain radar and Parsivel disdrometer measurements, Meteorological Applications, 23, 40-49, 2016.

Kruger, A. and Krajewski, W. F.: Two-dimensional video disdrometer: A description, Journal of Atmospheric and Oceanic Technology, 19, 602-617, 2002.

Kunii, D.: 0. Levenspiel, Fluidization Engineering, John Wiley, 8, 44-45, 1969.

Langmann, B., Folch, A., Hensch, M., and Matthias, V.: Volcanic ash over Europe during the eruption of Eyjafjallajökull on Iceland, April–May 2010, Atmospheric Environment, 48, 1-8, 2012.

Maki, M. and Doviak, R.: Volcanic ash size distribution determined by weather radar, 2001, 1810-1811.

Maki, M., Iguchi, M., Maesaka, T., Miwa, T., Tanada, T., Kozono, T., Momotani, T., Yamaji, A., and Kakimoto, I.: Preliminary results of weather radar observations of sakurajima volcanic smoke, Journal of Disaster Research, 11, 15-30, 2016.

Maki, M., Maesaka, T., Kozono, T., Nagai, M., Furukawa, R., Nakada, S., Koshida, T., and Takenaka, H.: Quantitative volcanic ash estimation by operational polarimetric weather radar, 2012.

Maki, M., Maesaka, T., Muraji, Y., and Suzuki, I.: Statistical analysis of volcanic ash measured by X-band polarimetric radar, 2014.

Mandø, M. and Rosendahl, L.: On the motion of non-spherical particles at high Reynolds number, Powder Technology, 202, 1-13, 2010.

Marzano, F. S., Barbieri, S., Vulpiani, G., and Rose, W. I.: Volcanic ash cloud retrieval by ground-based microwave weather radar, IEEE transactions on geoscience and remote sensing, 44, 3235-3246, 2006.

Marzano, F. S., Picciotti, E., Montopoli, M., and Vulpiani, G.: Inside volcanic clouds: Remote sensing of ash plumes using microwave weather radars, Bulletin of the American Meteorological Society, 94, 1567-1586, 2013.

Marzano, F. S., Picciotti, E., Vulpiani, G., and Montopoli, M.: Synthetic signatures of volcanic ash cloud particles from X-band dual-polarization radar, IEEE Transactions on Geoscience and Remote Sensing, 50, 193-211, 2012.

Matson, R. J. and Huggins, A. W.: The direct measurement of the sizes, shapes and kinematics of falling hailstones, Journal of the Atmospheric Sciences, 37, 1107-1125, 1980.

Nešpor, V., Krajewski, W. F., and Kruger, A.: Wind-induced error of raindrop size distribution measurement using a two-dimensional video disdrometer, Journal of Atmospheric and Oceanic Technology, 17, 1483-1492, 2000.

Miwa T., Maki M., Kozono T., Fujita E., Tanada T., and Iguchi M.: Experimental measurement on falling velocity of volcanic ash from Sakurajima volcano by using PARSIVEL disdrometer. Annual of Disas. Prev. Res. Inst., Kyoto Univ. 58(B), 91-94, 2015.

Oguchi, T., Udagawa, M., Nanba, N., Maki, M., and Ishimine, Y.: Measurements of dielectric constant of volcanic ash erupted from five volcanoes in Japan, IEEE Transactions on Geoscience and Remote Sensing, 47, 1089-1096, 2009.

Poulidis, A. P., Takemi, T., Iguchi, M., and Renfrew, I. A.: Orographic effects on the transport and deposition of volcanic ash: A case study of Mount Sakurajima, Japan, Journal of Geophysical Research: Atmospheres, 122, 9332-9350, 2017.

Pruppacher, H. R. and Beard, K.: A wind tunnel investigation of the internal circulation and shape of water drops falling at terminal velocity in air, Quarterly Journal of the Royal Meteorological Society, 96, 247-256, 1970.

Riley, C. M., Rose, W. I., and Bluth, G. J.: Quantitative shape measurements of distal volcanic ash, Journal of Geophysical Research: Solid Earth, 108, 2003.

Rong, L., Zhou, Z., and Yu, A.: Lattice–Boltzmann simulation of fluid flow through packed beds of uniform ellipsoids, Powder Technology, 285, 146-156, 2015.

Rosenfeld, D. and Ulbrich, C. W.: Cloud microphysical properties, processes, and rainfall estimation opportunities. In: Radar and Atmospheric Science: A Collection of Essays in Honor of David Atlas, Springer, 2003.

Ryzhkov, A., Pinsky, M., Pokrovsky, A., and Khain, A.: Polarimetric radar observation operator for a cloud model with spectral microphysics, Journal of Applied Meteorology and Climatology, 50, 873-894, 2011.

Sauvageot, H.: Radar meteorology, Artech House Publishers, 1992.

Seliga, T. A. and Bringi, V.: Potential use of radar differential reflectivity measurements at orthogonal polarizations for measuring precipitation, Journal of Applied Meteorology, 15, 69-76, 1976.

Seligman, A. N., Bindeman, I. N., Watkins, J. M., and Ross, A. M.: Water in volcanic glass: From volcanic degassing to secondary hydration, Geochimica et Cosmochimica Acta, 191, 216-238, 2016.

Sigurdsson, H., Houghton, B., McNutt, S., Rymer, H., and Stix, J.: The encyclopedia of volcanoes, Elsevier, 2015.

Sparks, R., Bursik, M., Carey, S., Gilbert, J., Glaze, L., Sigurdsson, H., and Woods, A.: Volcanic Plumes, 574 pp. John Wiley, Chichester, UK, 1997.

Stevenson, J., Millington, S., Beckett, F., Swindles, G., and Thordarson, T.: Big grains go far: understanding the discrepancy between tephrochronology and satellite infrared measurements of volcanic ash, Atmospheric Measurement Techniques, 8, 2069-2091, 2015.

Stokes, G. G.: On the effect of the internal friction of fluids on the motion of pendulums, Pitt Press Cambridge, 1851.

Suzuki, T.: A theoretical model for dispersion of tephra, Arc volcanism: physics and tectonics, 95, 113, 1983.

Tajima, Y., Ohara, D., Fukuda, K., and Shimomura, S.: Development of Automatic Tephrometer for Monitoring of Volcano, 2015, 39-46.

Testud, J., Oury, S., Black, R. A., Amayenc, P., and Dou, X.: The concept of “normalized” distribution to describe raindrop spectra: A tool for cloud physics and cloud remote sensing, Journal of Applied Meteorology, 40, 1118-1140, 2001.

Thurai, M. and Bringi, V.: Drop axis ratios from a 2D video disdrometer, Journal of Atmospheric and Oceanic Technology, 22, 966-978, 2005.

Thurai, M., Huang, G., Bringi, V., Randeu, W., and Schönhuber, M.: Drop shapes, model comparisons, and calculations of polarimetric radar parameters in rain, Journal of Atmospheric and Oceanic Technology, 24, 1019-1032, 2007.

Tokay, A., Wolff, D. B., and Petersen, W. A.: Evaluation of the new version of the laser-optical disdrometer, OTT Parsivel2, Journal of Atmospheric and Oceanic Technology, 31, 1276-1288, 2014.

Tran-Cong, S., Gay, M., and Michaelides, E. E.: Drag coefficients of irregularly shaped particles, Powder Technology, 139, 21-32, 2004.

Ulbrich, C. W.: Natural variations in the analytical form of the raindrop size distribution, Journal of Climate and Applied Meteorology, 22, 1764-1775, 1983.

Van Eaton, A. R., Muirhead, J. D., Wilson, C. J., and Cimarelli, C.: Growth of volcanic ash aggregates in the presence of liquid water and ice: an experimental approach, Bulletin of volcanology, 74, 1963-1984, 2012.

Waterman, P.: Matrix formulation of electromagnetic scattering, Proceedings of the IEEE, 53, 805-812, 1965.

Waterman, P. C.: Symmetry, unitarity, and geometry in electromagnetic scattering, Physical review D, 3, 825, 1971.

Wilson, L. and Huang, T.: The influence of shape on the atmospheric settling velocity of volcanic ash particles, Earth and Planetary Science Letters, 44, 311-324, 1979.

Wilson, T. M., Jenkins, S., and Stewart, C.: Impacts from volcanic ash fall. In: Volcanic Hazards, Risks and Disasters, Elsevier, 2015.

Wilson, T. M., Stewart, C., Sword-Daniels, V., Leonard, G. S., Johnston, D. M., Cole, J. W., Wardman, J., Wilson, G., and Barnard, S. T.: Volcanic ash impacts on critical infrastructure, Physics and Chemistry of the Earth, Parts A/B/C, 45, 5-23, 2012.

Figures

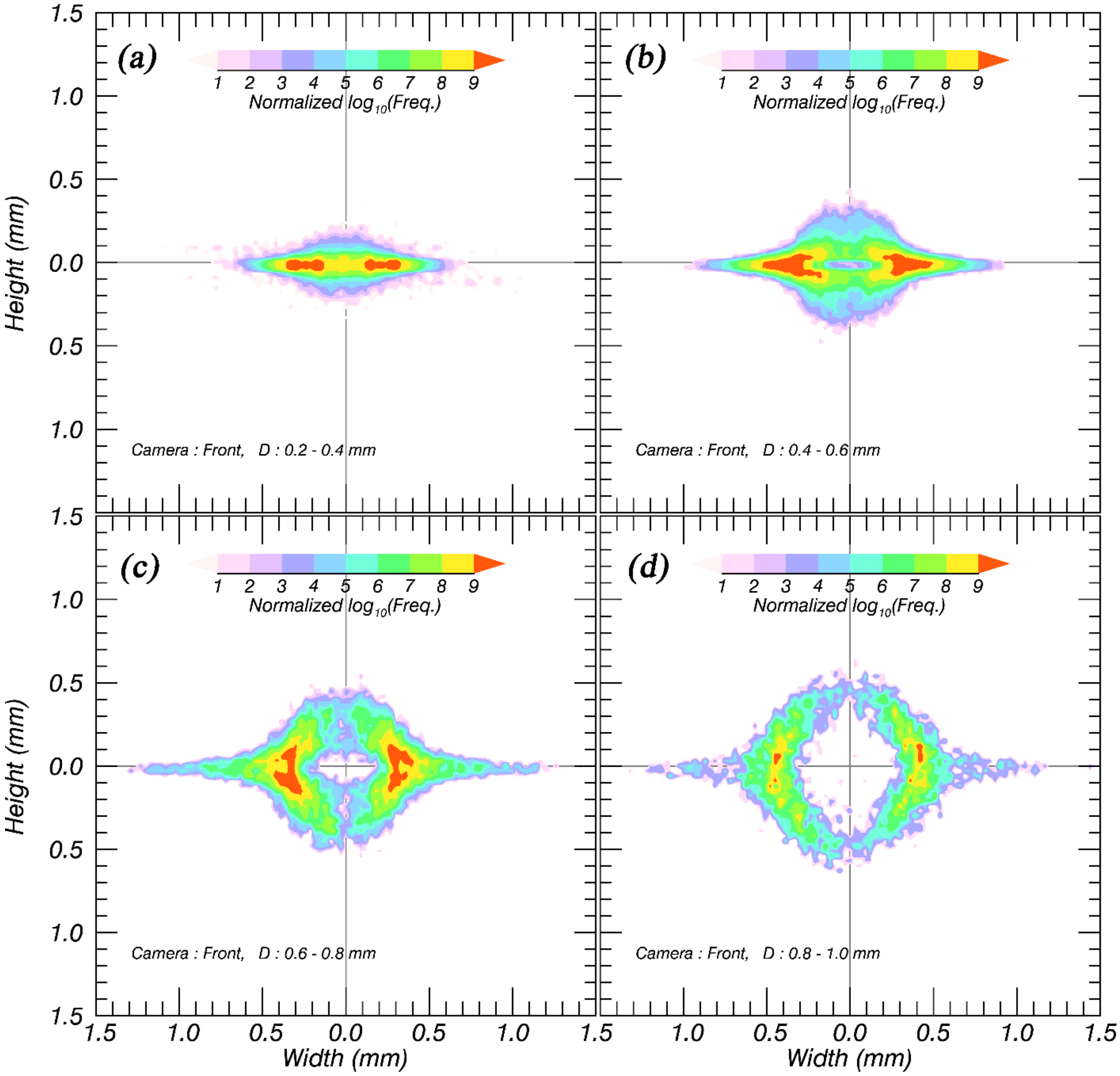

Figure 1. Accumulated contoured images of volcanic ash particles with D measured by a two-dimensional video disdrometer (2DVD).

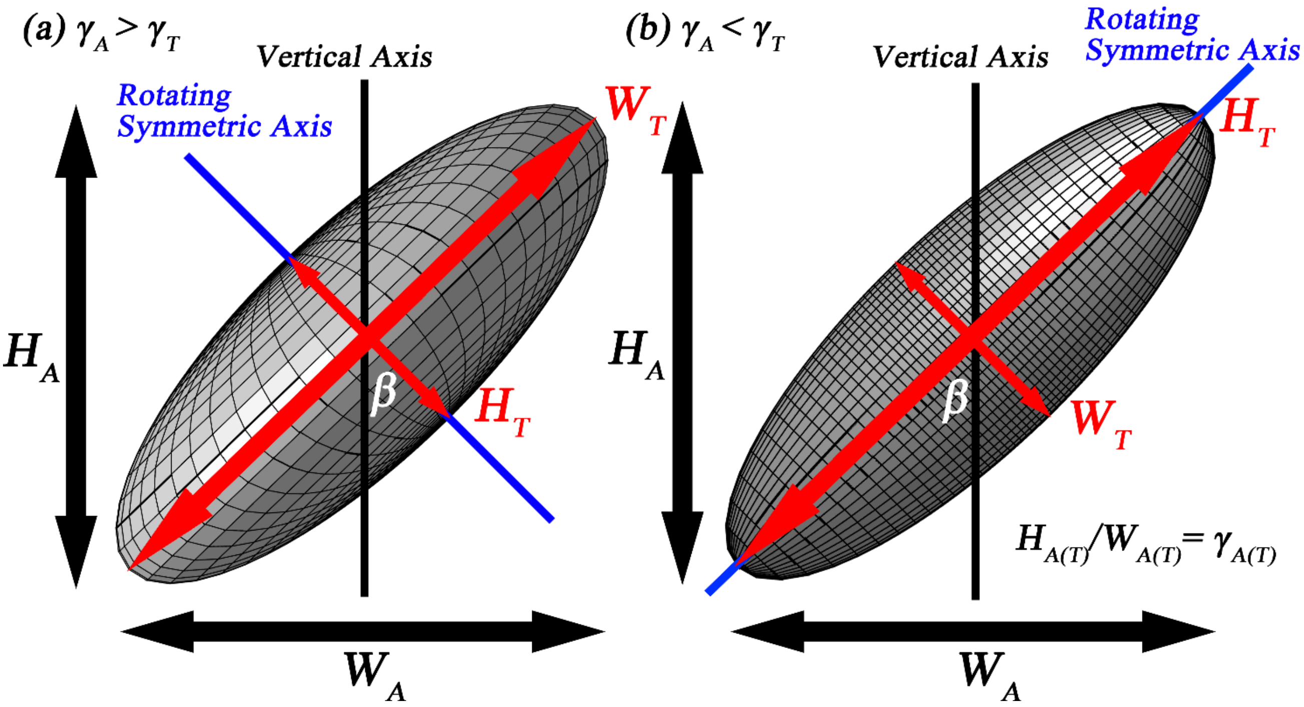

Figure 2. Conceptual model of an (a) oblate and (b) prolate spheroid with the same canting angle (β). $W_{A(T)}$ and $H_{A(T)}$ are the apparent (true) width and height of the particle, respectively. $\gamma_{A(T)}$ is the apparent (true) axis ratio.

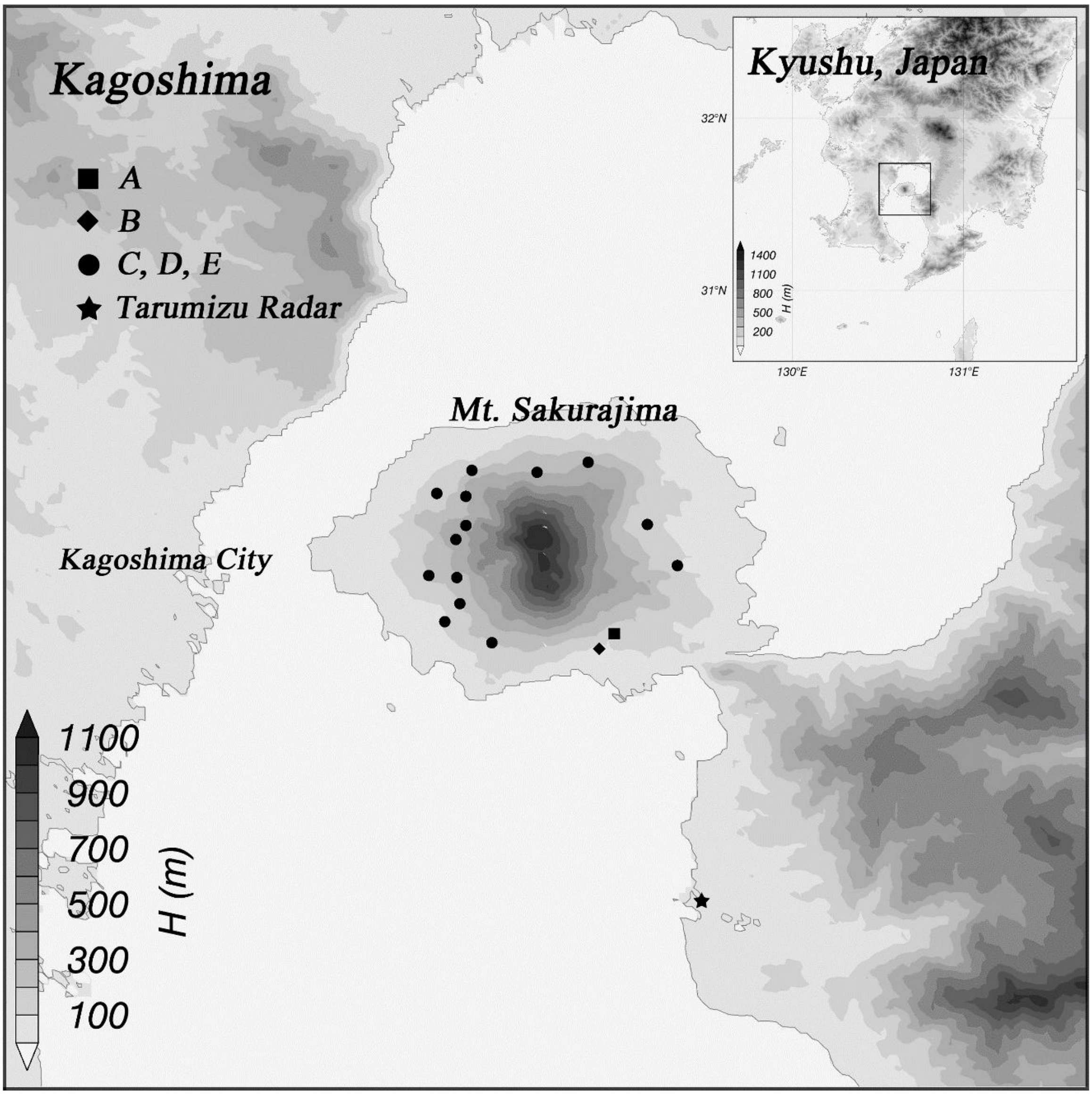

Figure 3. The locations of tephrometers and Showa crater on Sakurajima volcano, Japan. Black symbols indicate the locations of tephrometers and the star, square, and circle symbols correspond to datasets A, B and C–E, respectively. The white circle symbol represents the location of Showa crater.

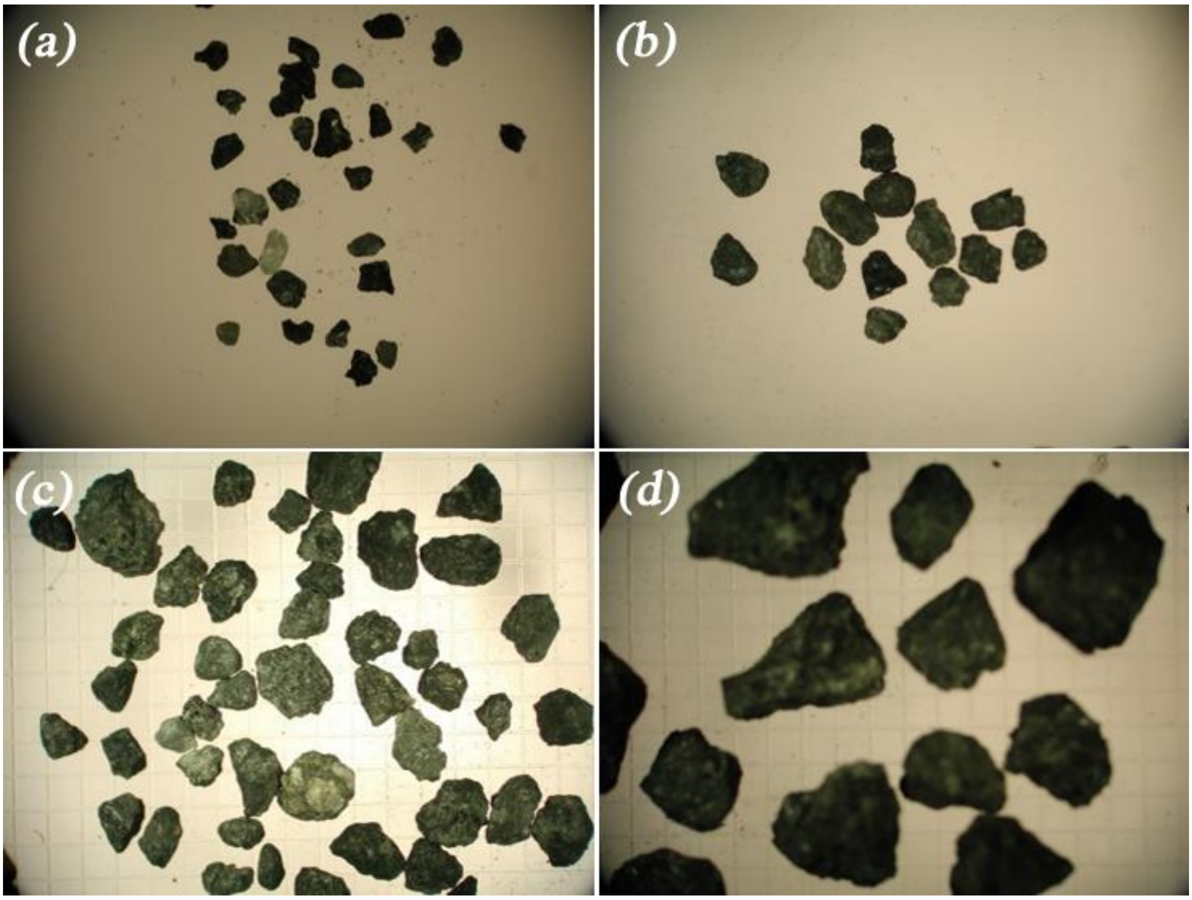

Figure 4. Real images of volcanic ash particles used in the present study. The particles were classified as (a) 0.125 mm < D ≤ 0.25 mm, (b) 0.25 mm < D ≤ 1 mm, (c) 1 mm < D < 2 mm, and (d) 2 < D ≤ 4 mm.

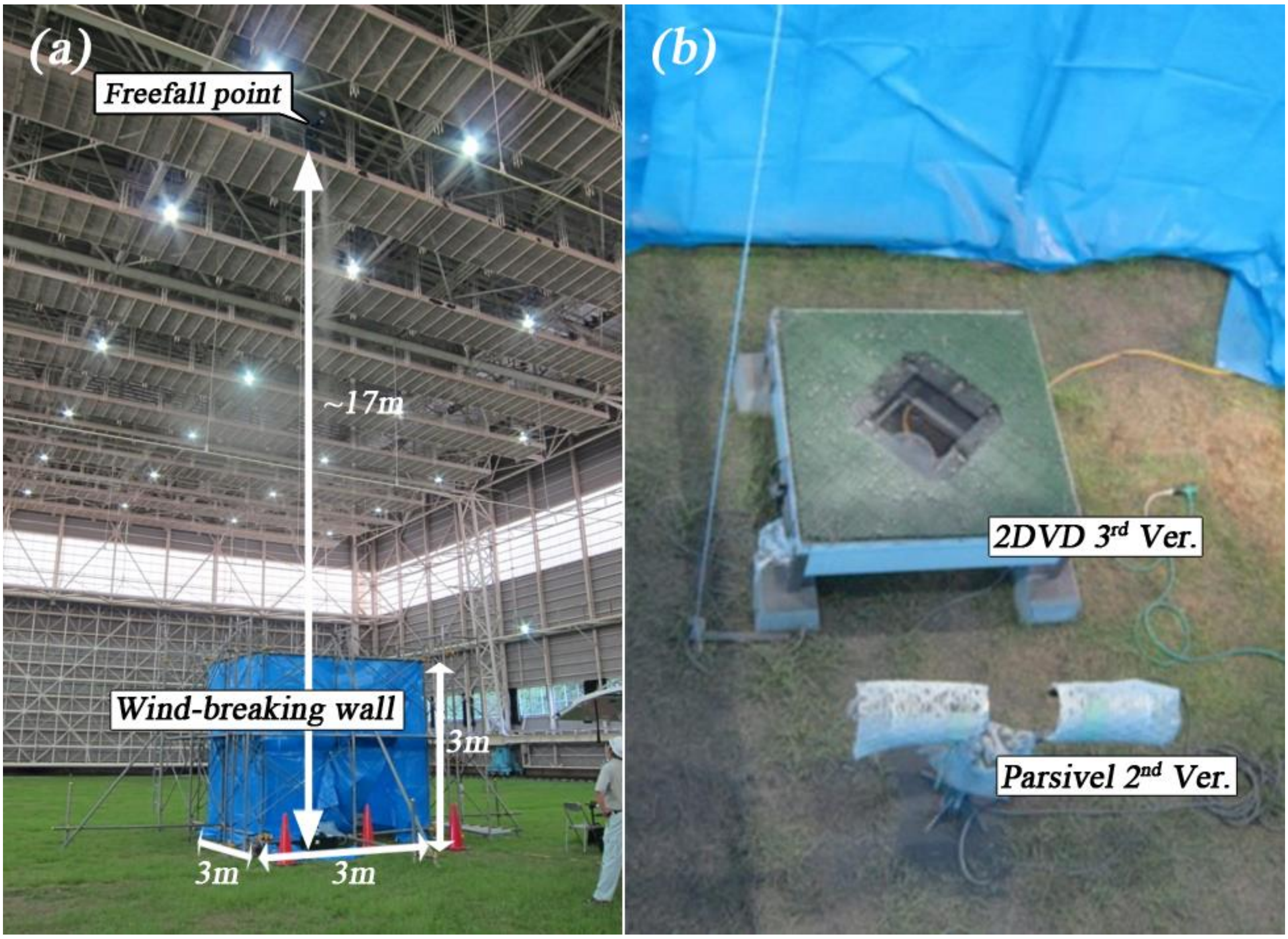

Figure 5. Free-fall experiment conditions of volcanic ash particles on the (a) outside and (b) inside of the wind-breaking wall covering the disdrometers in the large-scale rainfall simulator of the National Research Institute for Earth Science and Disaster Prevention (NIED).

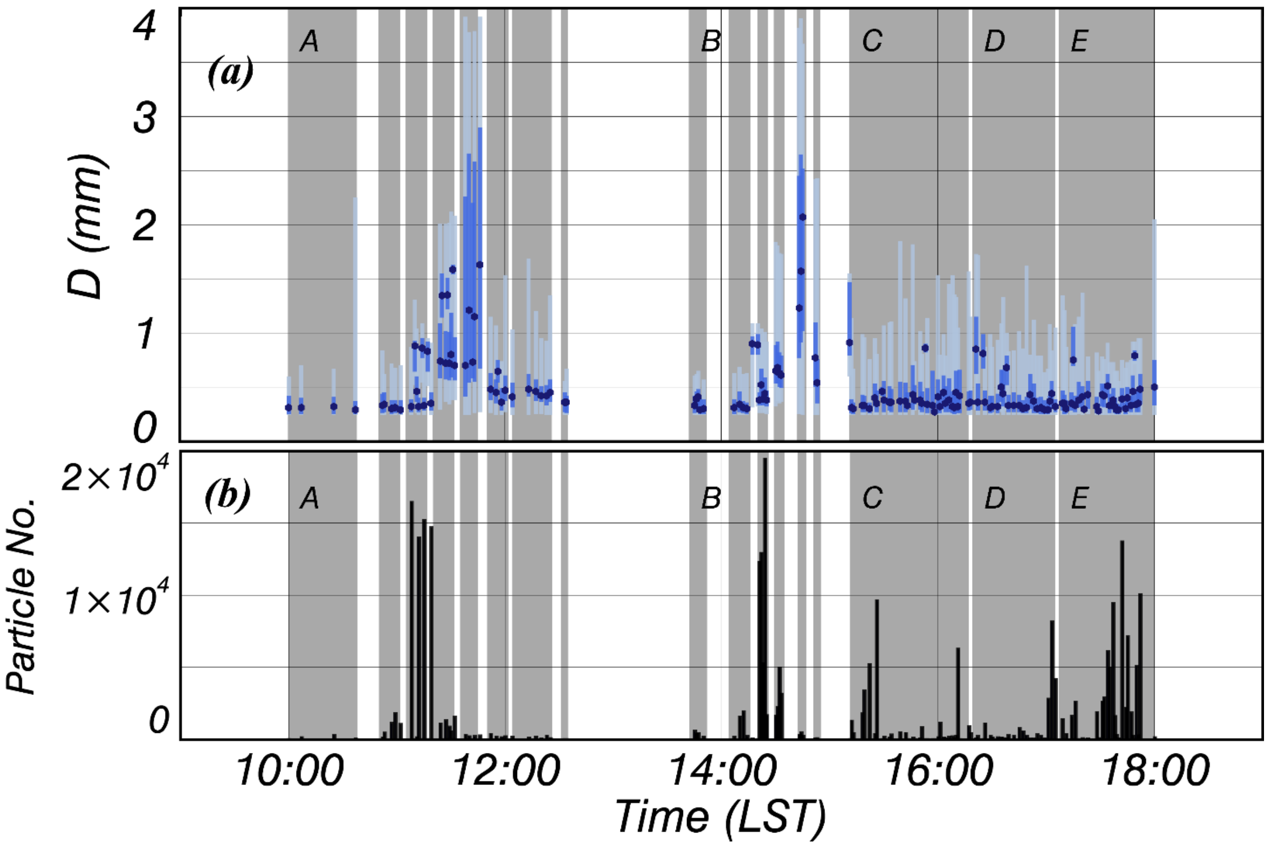

Figure 6. The 1-min interval time series of D and the number of particles in the free-fall experiment conducted at the NIED.

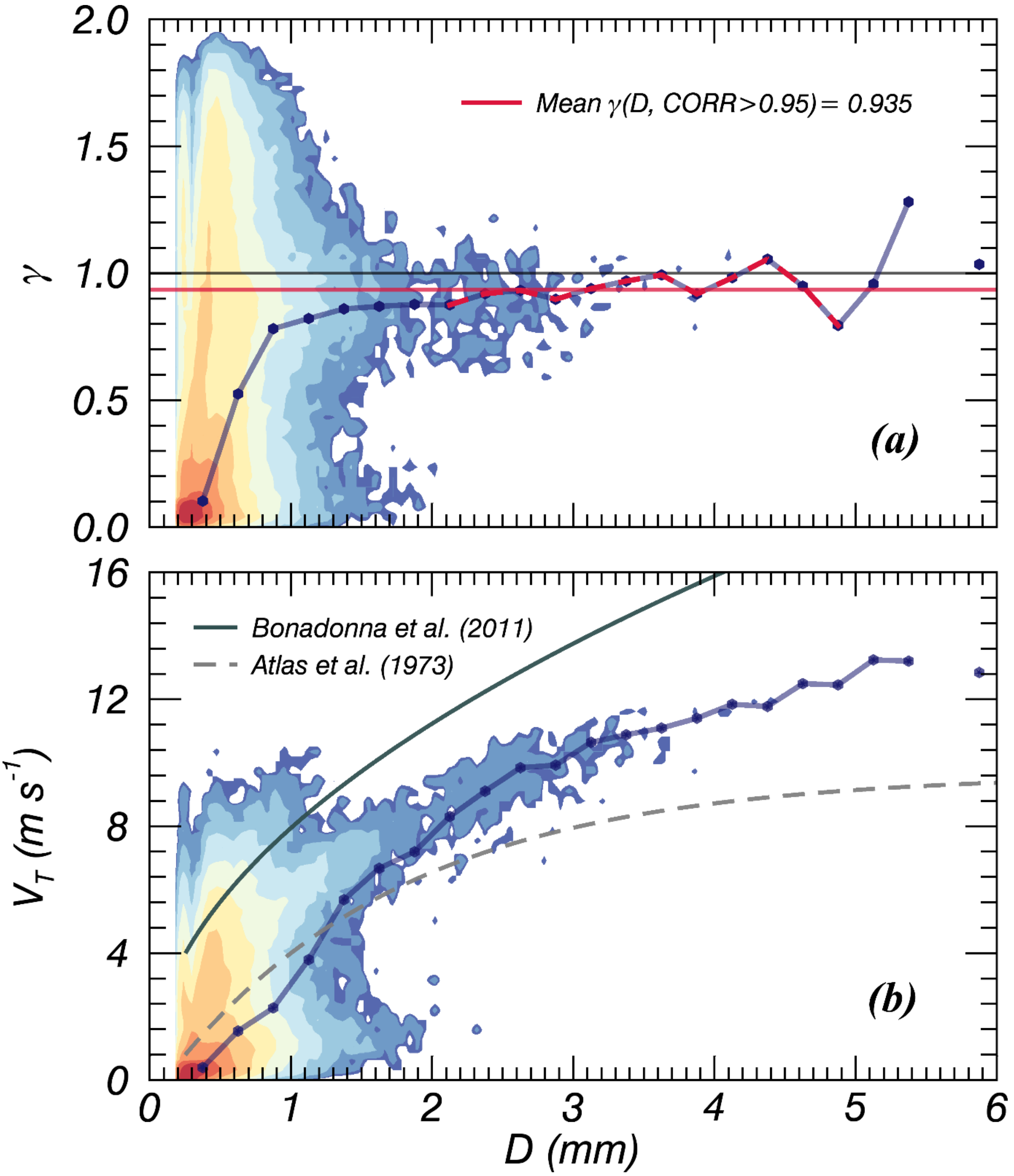

Figure 7. Contour image of volcanic ash particles for (b) the axis ratio (γ) and (b) terminal velocity (V_T) with respect to the raw data. Grey solid and broken lines are the relationships between volcanic ash particles and raindrops suggested by Bonadonna et al. (2011) and Atlas et al. (1971), respectively. The red solid line is the averaged γ satisfying the condition that the correlation coefficient exceeds 0.95.

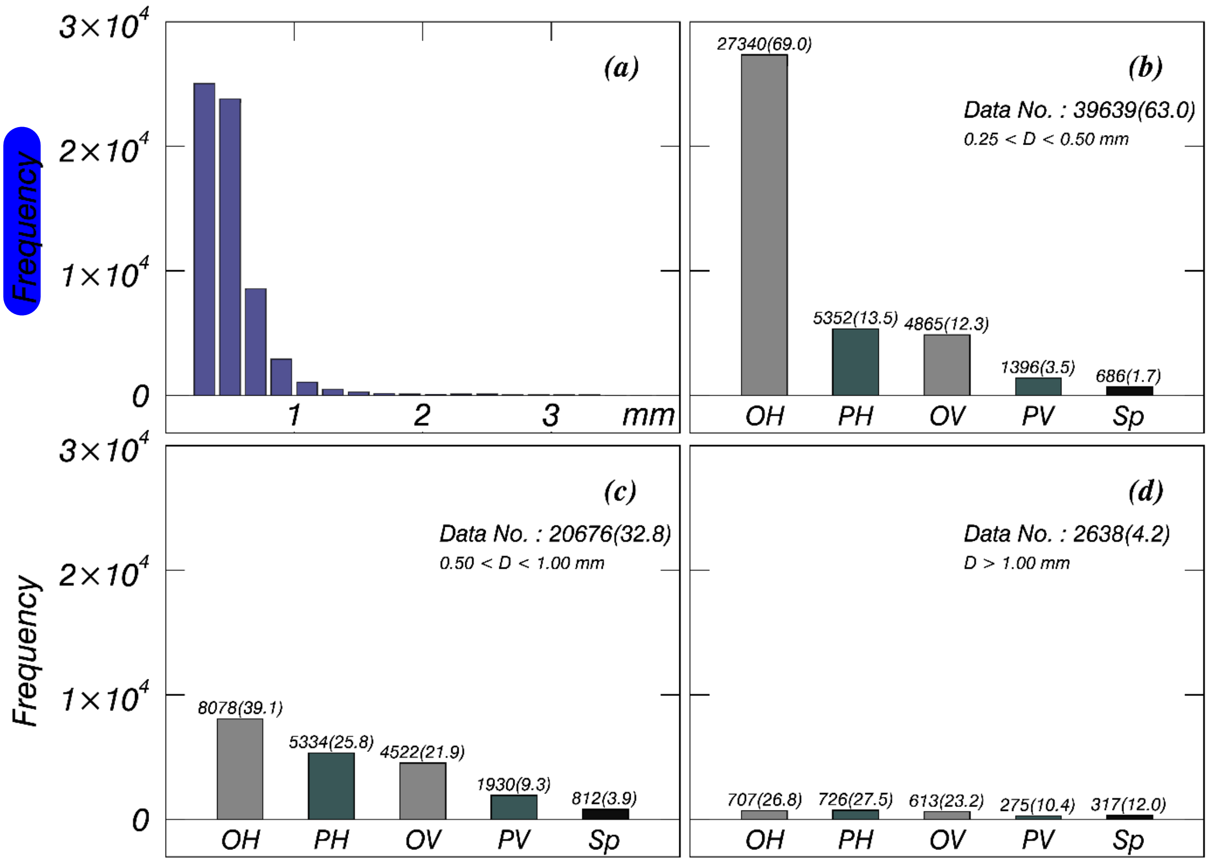

Figure 8. Histograms of volcanic ash particles for (a) all particle types and (b–d) each particle shape type of the phi scale. The grey- and dark grey-shaded (patterned) bars indicate horizontal oblate (OH) (vertical oblate [OV]) and horizontal prolate (PH) (vertical prolate [PV]), respectively. The black bar corresponds to spherical (Sp) particles. The number on the top of each bar plot is the number of data points and that in parenthesis is the percentage for each phi scale.

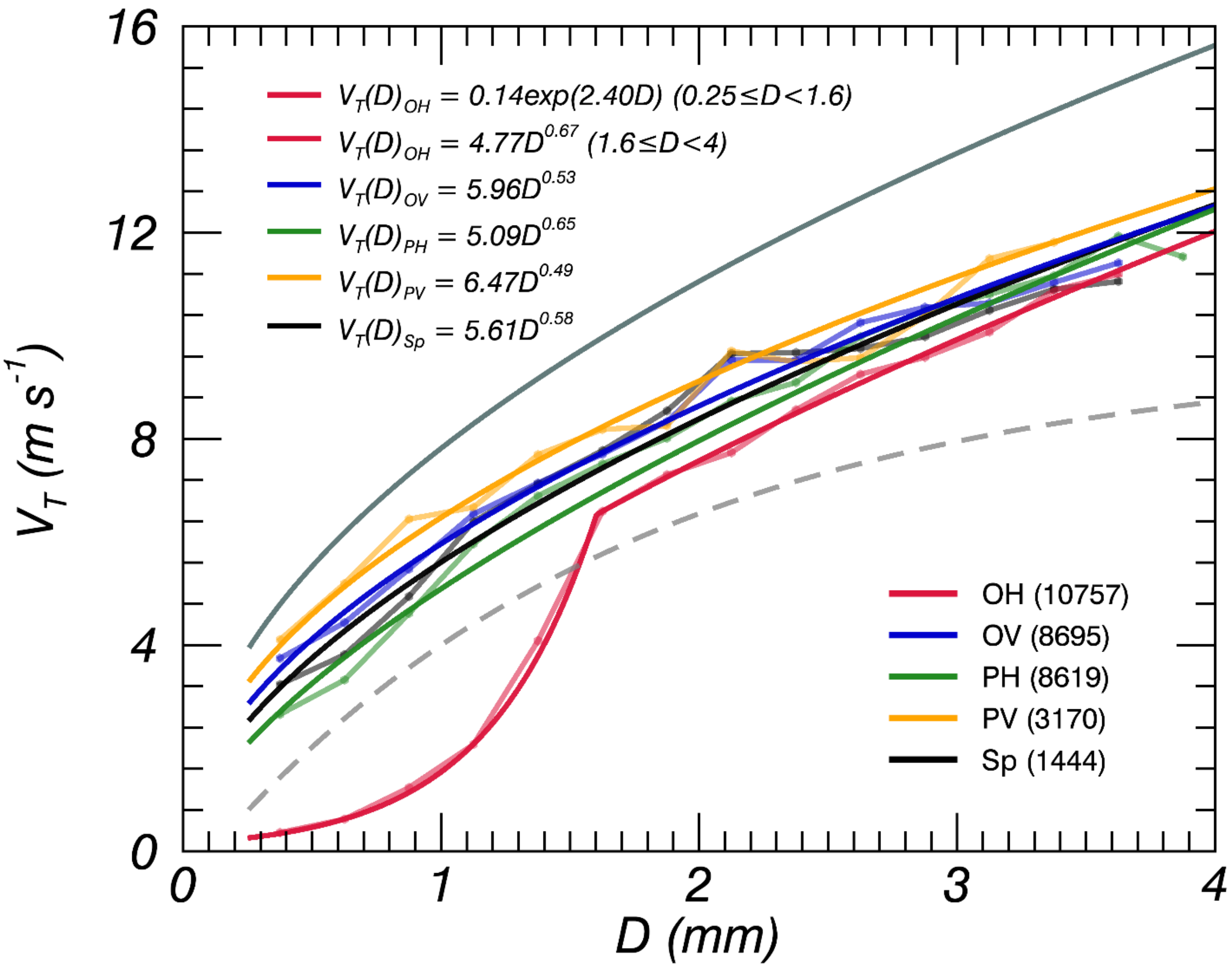

Figure 9. Distribution of median V_T values after applying a 60% V_T quality control (QC) threshold for each particle shape type. The grey solid and broken lines show the relationships of volcanic ash particles and raindrops suggested by Bonadonna et al. (2011) and Atlas et al. (1971), respectively.

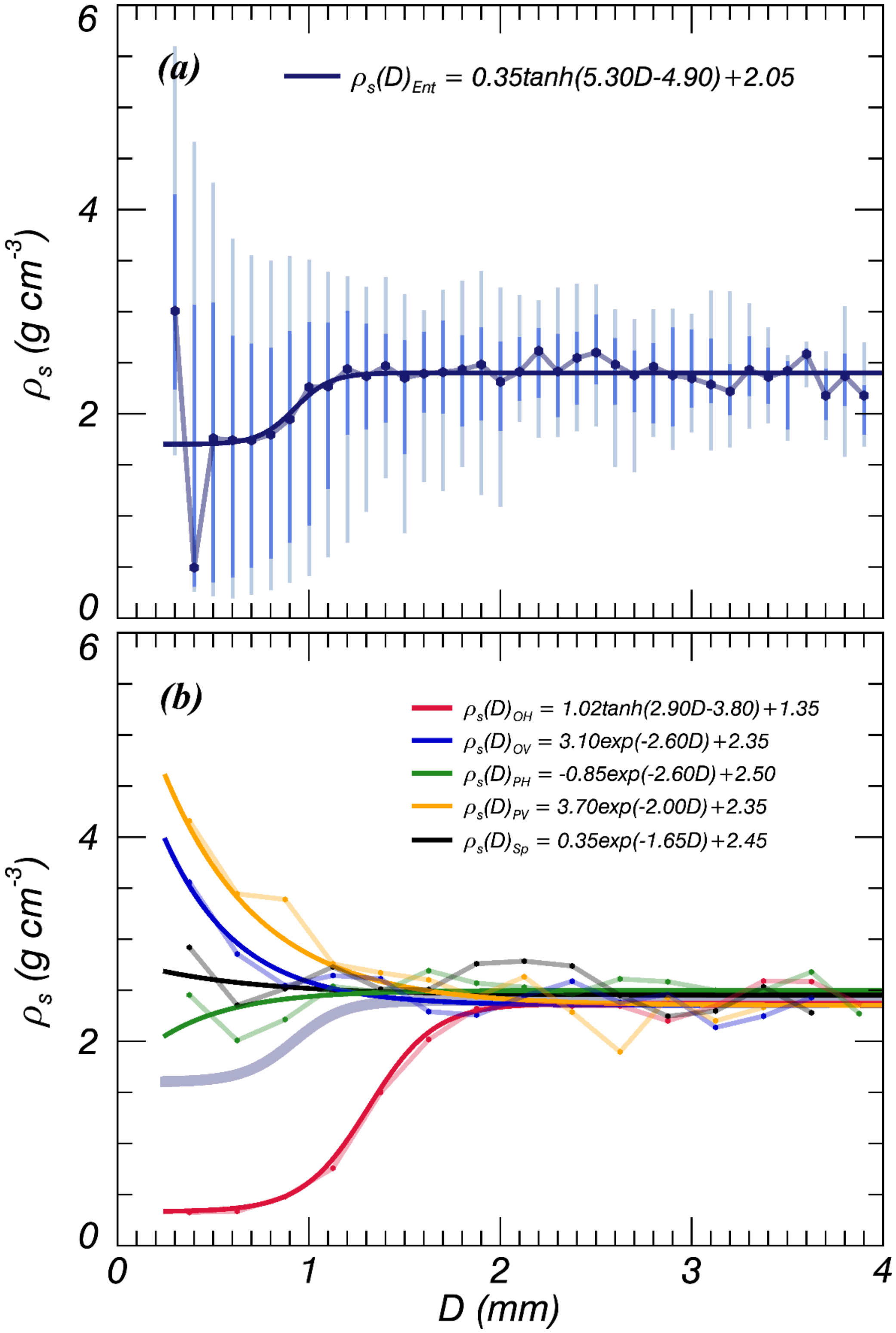

Figure 10. Distribution of (a) quartile and (b) median particle density (ρ_s) values after applying the 60% V_T QC threshold for all, and each individual, particle shape type, respectively.

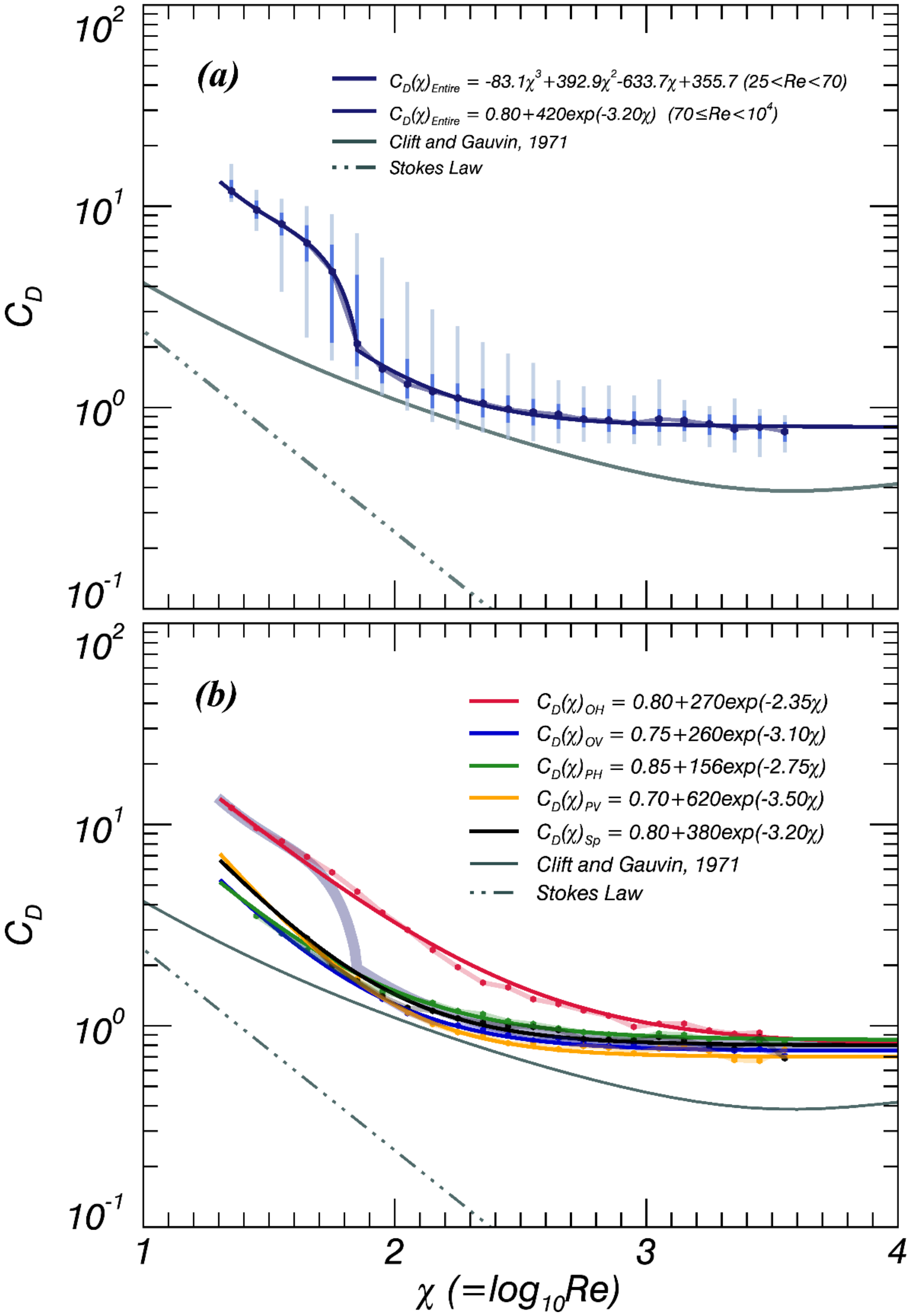

Figure 11. Same as Fig. 10 but for Reynolds number (Re) and drag coefficient (C_D). The grey solid and broken lines in (a) are the relationships of spheres suggested by Clift and Gauvin (1971) and Stokes (1851), respectively.

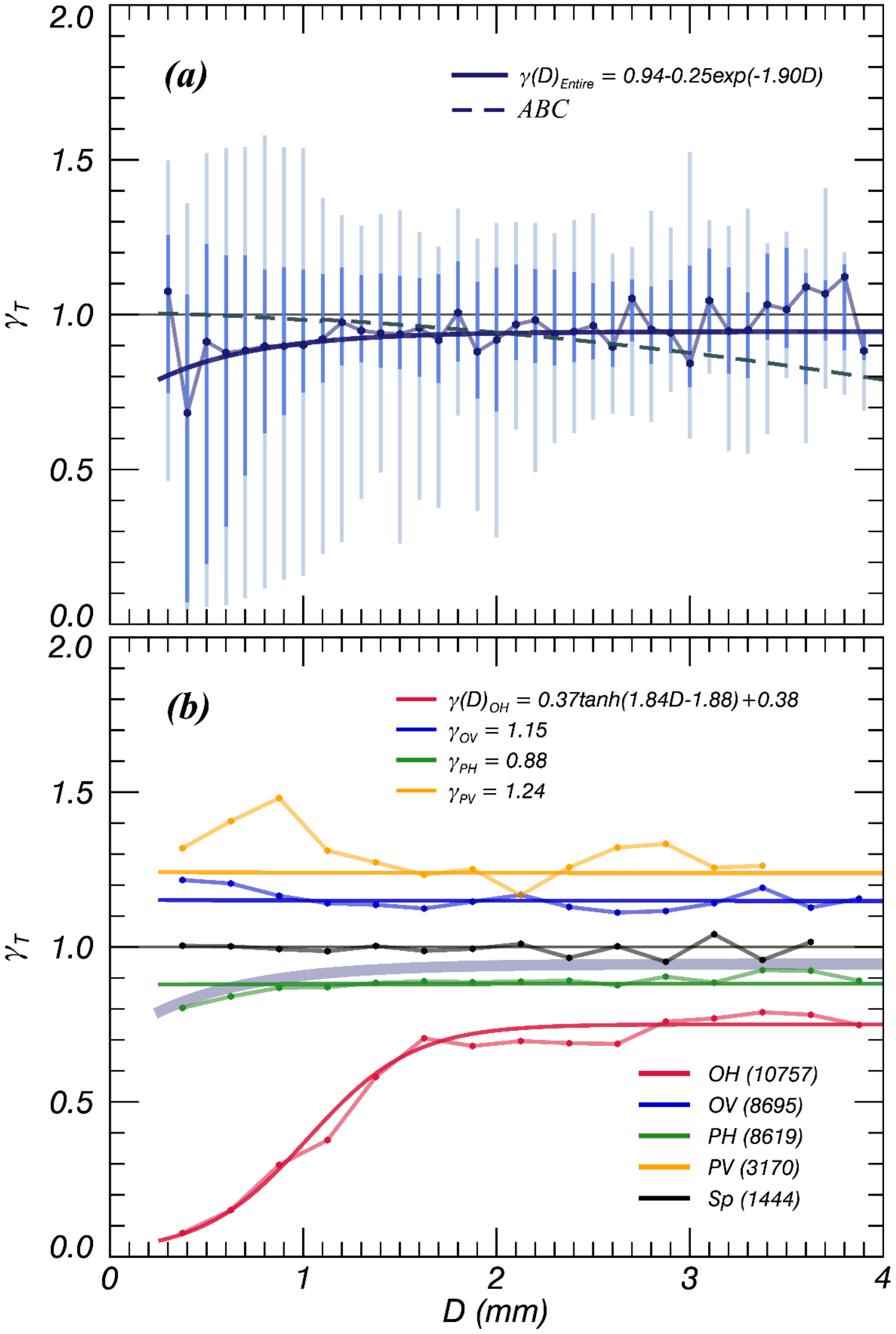

Figure 12. Same as Fig. 10 but for γ. The grey broken line (ABC) in (a) shows the relationships of γ for raindrops suggested by Beard and Chuang (1987) and Andsager et al. (1999).

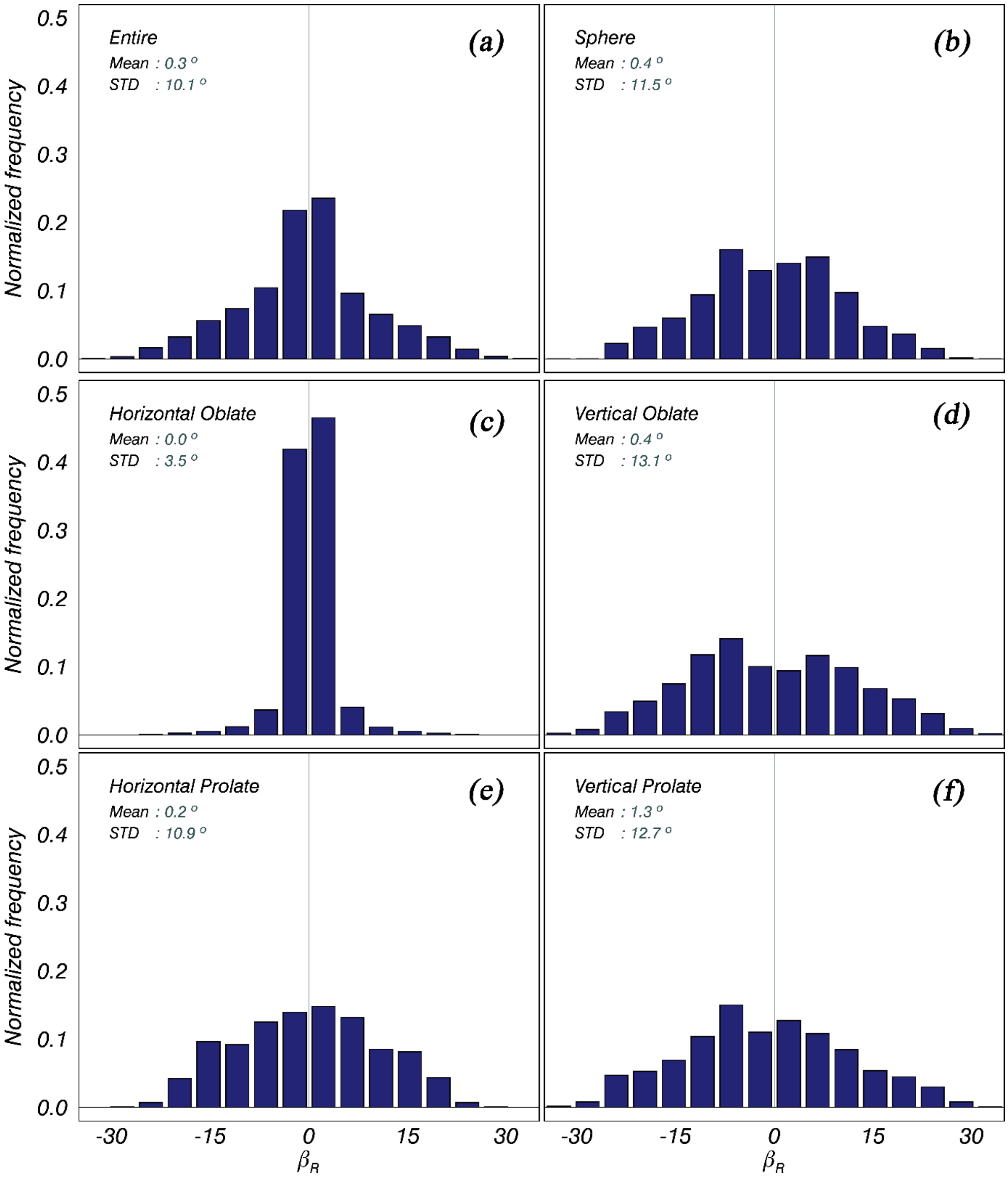

Figure 13. Histograms of representative canting angle (β_R) for each particle shape type, including the data for all particles.

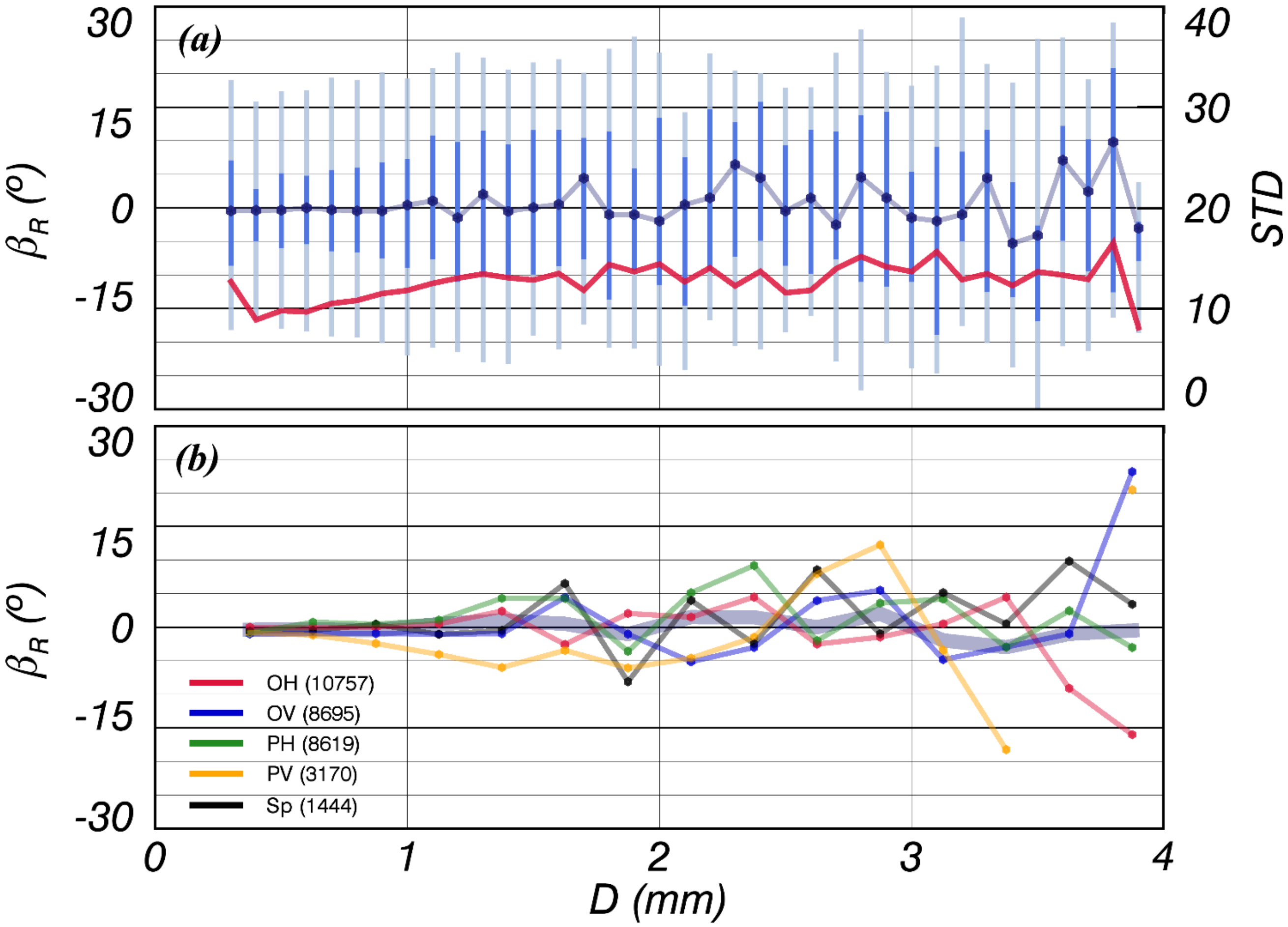

Figure 14. Distribution of β_R with D for each particle shape type including the data for all particles. The red solid line indicates the standard deviation.

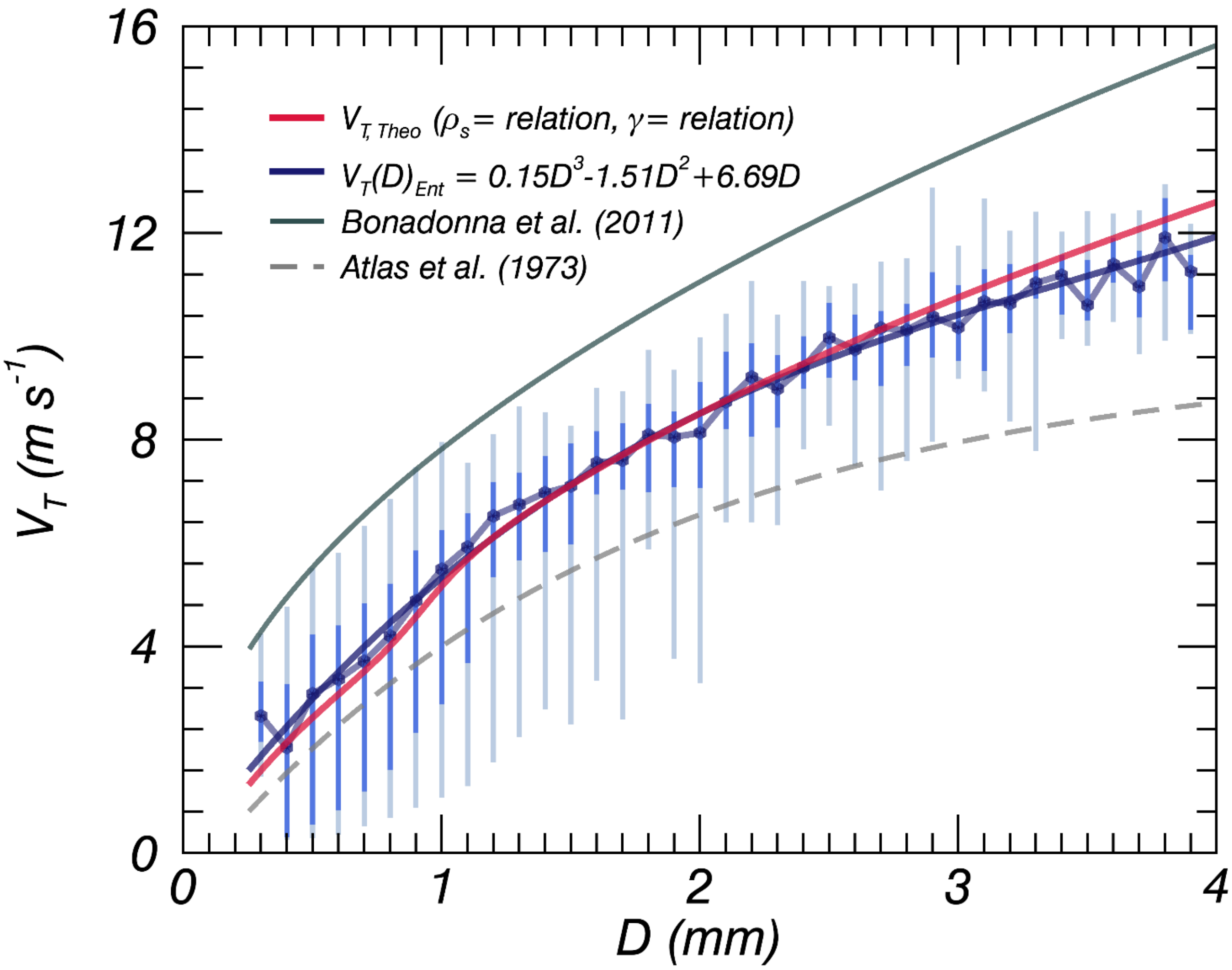

Figure 15. The V_T quartiles after applying the 60% V_T QC threshold for all, and each individual, particle shape type, respectively. Grey solid and broken lines in (a) are the relationships of volcanic ash particles and raindrops suggested by Bonadonna et al. (2011) and Atlas et al. (1971), respectively. The red solid line indicates the $V_{T,Ref}$ relationships of γ and particle density suggested by the present study.

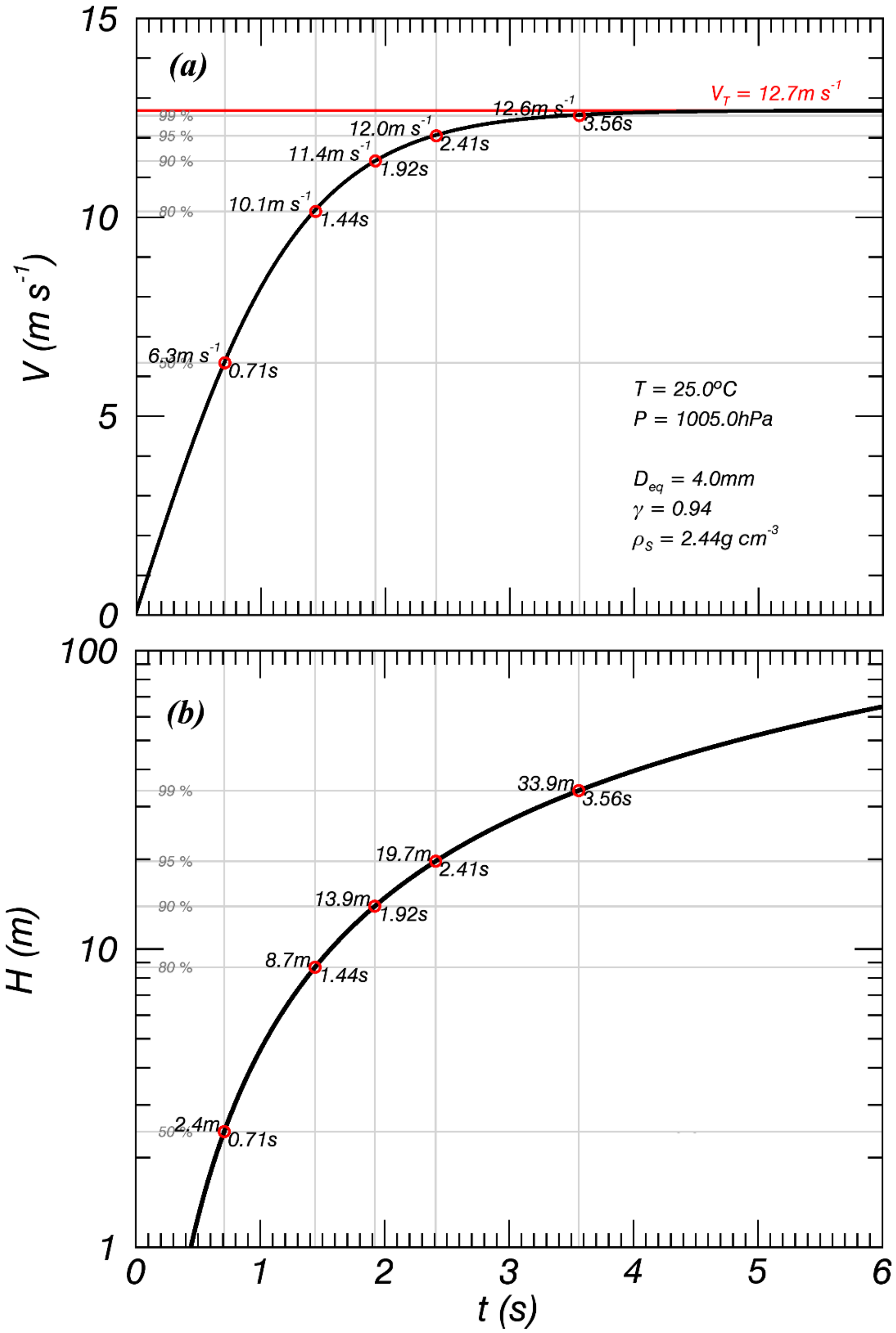

Figure A1. Theoretical (a) fall velocity and (b) falling height for a sphere with D = 4 mm, considering the surface roughness coefficient of the volcanic ash particle (1.07^{-1}) relative to its fall velocity (Bagheri and Bonadonna, 2016).

Tables

Table 1. Particle number by particle shape type after applying quality controls and ash particle classification criteria.

Type	Description	Classification conditions	Data number (%)
All	All	.	62,953 (100)
OH	Horizontal oblate	$\gamma_{T1(2)} < 0.9$ $\lvert\gamma_{T1} - \gamma_{T2}\rvert \leq 0.1\gamma_T$	36,125 (57.38)
OV	Vertical oblate	$0.9 \leq \gamma_{T1(2)} \leq 1.1,$ $\gamma_{T2(1)} > 1.1$	10,000 (15.88)
PH	Horizontal prolate	$\lvert\gamma_{T1} - \gamma_{T2}\rvert > 0.1\gamma_T$	11,412 (18.13)
PV	Vertical prolate	$\gamma_{T1(2)} > 1.1$ $\lvert\gamma_{T1} - \gamma_{T2}\rvert \leq 0.1\gamma_T$	3,601 (5.72)
Sp	Sphere	$0.9 \leq \gamma_{T1(2)} \leq 1.1$ $\lvert\gamma_{T1} - \gamma_{T2}\rvert \leq 0.1\gamma_T$	1,815 (2.88)

Table 2. Information on the collected volcanic ash particles.

Data	Collection date	Re-analysis time (June 18, 2014)	Re-analysis method
A	Dec. 1–31 2008	10:00–12:34 (154 min)	Size by size (phi scale)
B	Mar. 1–31 2010	13:43–14:53 (70 min)	Size by size (phi scale)
C	Feb. 28, 2014	15:11–16:17 (66 min)	Mixed
D	Mar. 31, 2014	16:19–17:05 (46 min)	Mixed
E	Apr. 30 2014	17:07–18:00 (53 min)	Mixed

Table 3. Relationships of terminal velocity with the number of data points, the value of the correlation coefficient (CC) and the root mean square error (RMSE) after applying the 60% V_T QC threshold for each particle shape type.

Type	**Data number (%)**	**Relationship ($0.25 < D$ (mm) ≤ 4)**	**CC**	**RMSE**
All	32685 (100)	$V_T(D) = 0.15D^3-1.51D^2+6.69D$	0.56	1.22
OH	10757 (34.12)	$V_T(D) = 0.14\exp(2.40D)$ ($0.25 \leq D < 1.6$) $V_T(D) = 4.77D^{0.67}$ ($1.6 \leq D < 4$)	0.94	0.46
OV	8695 (26.60)	$V_T(D) = 5.96D^{0.53}$	0.75	0.85
PH	8619 (26.36)	$V_T(D) = 5.09D^{0.65}$	0.87	0.74
PV	3170 (9.69)	$V_T(D) = 6.47D^{0.49}$	0.71	0.96
Sp	1444 (4.41)	$V_T(D) = 5.61D^{0.56}$	0.91	0.78